The Intra-Seasonal Oscillation and its control of tropical cyclones simulated by high-resolution global atmospheric models

M. Satoh · K. Oouchi · T. Nasuno · H. Taniguchi · Y. Yamada ·
H. Tomita · C. Kodama · J. Kinter · D. Achuthavarier ·
J. Manganello · B. Cash · T. Jung · T. Palmer · N. Wedi

Abstract Project Athena is an international collaboration testing the efficacy of high-resolution global climate models. We compare results from 7-km mesh experiments of the Nonhydrostatic Icosahedral Atmospheric Model (NICAM) and 10-km mesh experiments of the Integrated Forecast System (IFS), focusing on the Intra-Seasonal Oscillation (ISO) and its relationship with tropical cyclones (TC) among the boreal summer period (21 May–31 Aug) of 8 years (2001–2002, 2004–2009). In the first month of simulation, both models capture the intra-seasonal oscillatory behavior of the Indian monsoon similar to the observed boreal summer ISO in approximately half of the 8-year samples. The IFS simulates the NW–SE-oriented rainband and the westerly location better, while NICAM marginally reproduces mesoscale organized convective systems and better simulates the northward migration of the westerly peak and precipitation, particularly in 2006. The reproducibility of the evolution of MJO depends on the given year; IFS simulates the MJO signal well for 2002, while NICAM simulates it well for 2006. An empirical orthogonal function analysis shows that both models statistically reproduce MJO signals similar to observations, with slightly better phase speed reproduced by NICAM. Stronger TCs are simulated in NICAM than in IFS, and NICAM shows a wind-pressure relation for TCs closer to observations. TC cyclogenesis is active during MJO phases 3 and 4 in NICAM as in observations. The results show the potential of high-resolution global atmospheric models in reproducing some aspects of the relationship between MJO and TCs and the statistical behavior of TCs.

M. Satoh (✉)
Atmosphere and Ocean Research Institute,
The University of Tokyo, 5-1-5 Kashiwanoha,
Kashiwa-shi, Chiba 277-8568, Japan
e-mail: satoh@aori.u-tokyo.ac.jp

M. Satoh · K. Oouchi · T. Nasuno · Y. Yamada ·
H. Tomita · C. Kodama
Research Institute for Global Change,
Japan Agency for Marine-Earth Science and Technology,
3173-25 Showa-machi, Kanazawa-ku, Yokohama-shi,
Kanagawa 236-0001, Japan

H. Taniguchi
International Pacific Research Center, SOEST,
University of Hawaii at Manoa, Honolulu, HI, USA

H. Tomita
Advanced Institute for Computational Science/RIKEN,
7-1-26 Minatojima-minamimachi, Chuo-ku,
Kobe, Hyogo 650-0047, Japan

J. Kinter · D. Achuthavarier · J. Manganello · B. Cash
Center for Ocean-Land-Atmosphere Studies,
Calverton, MD, USA

T. Jung · T. Palmer · N. Wedi
European Centre for Medium-Range Weather Forecasts,
Shinfield Park, Reading RG2 9AX, UK

T. Jung
Alfred-Wegener-Institute for Polar and Marine Research,
P.O. Box 12 01 61, 27515 Bremerhaven, Germany

1 Introduction

The realistic simulation of the Intra-Seasonal Oscillation (ISO) that has a periodicity from a few weeks up to less than a season is a long-standing issue for global atmospheric circulation models (GCMs). Most GCMs have had

difficulty in reproducing the Madden–Julian Oscillation (MJO; Madden and Julian 1972), which is one manifestation of the ISO, until very recently (Slingo et al. 1996; Lin et al. 2006). Considerable efforts have been made to improve the ISO/MJO behavior within GCMs, particularly through the improvement of cumulus parameterization schemes (cf. Bechtold et al. 2008; Chikira and Sugiyama 2010) and also other model physics (Sperber and Annamalai 2008). Numerical Weather Prediction (NWP) modeling centers are interested in better reproducing the ISO/MJO since their signals are directly related to better skill scores for numerical weather forecasts of longer than 1 week (Gottschalck et al. 2010; Rashid et al. 2011). Some GCMs have shown improved forecasting skill for ISO, MJO, and TC (e.g. Kim et al. 2009). In addition, since MJO impacts tropical cyclone (TC) activity, a better representation of the MJO is crucial for realistic representation of tropical storms in numerical models (Vitart 2009).

Higher-resolution models that resolve deep convective motions explicitly are also expected to drive progress in representation of ISO/MJO based on the evidence of recent numerical experiments. Two types of global atmospheric models with explicit calculation of deep convection are: the multi-scale modeling framework (MMF, or super-parameterization), and global cloud-system resolving models (GCRM). The MMF, which is based on a coarse-resolution GCM with an embedded cloud-system model in each grid, is demonstrated to be promising to improve the simulation skill of Asian monsoon and MJO compared to currently available cumulus parameterization, in a given coupled atmosphere–ocean general circulation model (Stan et al. 2009). It also shows good statistical behavior of the MJO (Khairoutdinov et al. 2008; Benedict and Randall 2009). However, the MMF has not been shown to be suitable for the representation of the relation between MJO and TCs, likely because the host GCM is generally too coarse. The GCRM, which covers the Earth with a grid interval of around a few kilometers, shows the multi-scale structure of tropical convective systems (Tomita et al. 2005; Nasuno et al. 2007, 2009), and has been shown to simulate realistic behavior of an MJO event (Miura et al. 2007; Liu et al. 2009). The GCRM also realistically captured some aspects of the boreal summer ISO in the Indian Ocean (Oouchi et al. 2009b; Taniguchi et al. 2010). In addition, the higher resolution of the GCRM allows reproduction of many aspects of realistic TCs, especially intensity, since the threshold wind velocity used to define TCs needs not be artificially reduced when the horizontal resolution increases to around 10 km (Walsh et al. 2007).

A global high-resolution simulation with a mesh size of approximately 3.5 km using the Nonhydrostatic Icosahedral Atmospheric Model (NICAM; Sato et al. 2009; Tomita and Satoh 2004) showed realistic behavior of tropical cloud systems associated with diurnal to intra-seasonal variability

(Miura et al. 2007; Sato et al. 2009; Inoue et al. 2010). An interesting result from the NICAM simulations is that the behavior of the ISO/MJO bears some similarity with the observations, even as the mesh size is coarsened to approximately 7 and 14 km (Nasuno et al. 2009; Masunaga et al. 2008; Taniguchi et al. 2010), although such resolutions are not generally used for nonhydrostatic models. However, until recently, it has been difficult to perform a long-term simulation using NICAM to obtain the statistical behavior of ISO/MJO due to computer resource limitations.

The horizontal resolution of global atmospheric models of NWP centers have recently improved considerably, for example, the horizontal resolution of the Global Spectral Model (GSM) of the Japanese Meteorological Agency (JMA) was increased to 20 km in 2007, and that of Integrated Forecast System (IFS) of the European Centre for Medium-Range Weather Forecast (ECMWF) was increased to 16 km in 2010. These global forecast models are categorized as conventional GCMs using hydrostatic dynamics and cumulus parameterization schemes. The horizontal resolutions of these models became closer to those of NICAM (3.5, 7, or 14 km), so it is natural to investigate the similarity of the behavior of the ISO/MJO between these models. For this purpose, Project Athena was conceived (Kinter et al. 2011) and is discussed further in Sect. 2. Dirmeyer et al. (2011) compares the diurnal variations of precipitation from the simulations of Project Athena. The present study focuses on the behavior of the ISO/MJO and their relation to TCs simulated by the 10 km-mesh IFS and the 7 km-mesh NICAM. In Project Athena, various resolutions of IFS and the 7 km-mesh NICAM are used to perform several years of numerical simulation. In particular, the highest resolution IFS (10 km, or T2047) and the 7 km-mesh NICAM performed the same three-month (21 May–31 Aug) boreal summer simulations for 8 years (2001–2009, except for 2003).

The relation between MJO and TC within IFS has been examined by Vitart (2009) using an 80-km resolution operational model (TL255, Cy32r3). A series of hindcast runs were performed for the 20-year period of 1989–2008 with the hindcasts starting on the 15th of each month and spanning 46 days. For each starting date, the hindcasts consist of an ensemble of 15 members. In contrast, the statistical behavior of MJO within NICAM has not been studied, while the TC statistics generated by NICAM were documented by Yamada et al. (2010), who discuss the future projection of TC change simulated by the 14 km-mesh NICAM. In regards to case studies, Oouchi et al. (2009a) showed the relations between MJO and TCs in the boreal summer simulation of the year 2004 using the 7- and 14 km-mesh NICAM. Taniguchi et al. (2010) performed 14 km-mesh NICAM simulations of TC Nargis, which made landfall in Myanmar and caused severe damage in April 2008, and they argued that the ISO in the Indian

Ocean is closely related to the cyclogenesis of TC Nargis (see also Yanase et al. 2010). Taniguchi et al. (2010) further analyzed how cyclogenesis is modulated with the phases of MJO.

One purpose of the present study is to investigate how the relations between MJO and TC-genesis are reproduced in both the IFS and NICAM simulations. We particularly examine the relation to MJO, and not ISO in the Indian Ocean as discussed by Taniguchi et al. (2010) and Yanase et al. (2010), because the June-July–August season is not an active one for cyclones in the Indian Ocean.

The structure of the remainder of this paper is as follows. In Sect. 2, the background of Project Athena is concisely described, and the models and experimental setup are described in Sect. 3. In Sect. 4, after showing some aspects of simulated climatological fields, the behavior of the boreal summer ISO in the Indian Ocean is investigated. In particular, we focus on the northward propagation of convective systems in the Indian Ocean for the first month of each year. The statistical behavior of the ISO is described in Sect. 5 and statistical properties of TCs are presented in Sect. 6. Section 7 describes the relationships between MJO and TCs. Section 8 is devoted to a discussion, and summary and future issues are given in Sect. 9.

2 The scope of Project Athena and this paper

One of the motivations of the high-resolution model intercomparison project, Project Athena, is to explore the potential benefits and roles of high-resolution modeling we can expect in the seamless modeling of weather and climate, which is becoming possible with improving high-end computing resources (Kinter et al. 2011). A rationale for promoting such seamless modeling originates from the notion of handling weather and climate problem in a unified modeling framework (Shukla et al. 2009). Improvements in many modeling aspects are anticipated, including increase in resolution, the complexity of model components, and the length and ensemble numbers of simulation in order to obtain the most benefit from the synergy of high-resolution models and the computing resources now available. Through Project Athena, we explore the benefits of the state-of-the-art hydrostatic model (ECMWF-IFS; Bechtold et al. 2008; Jung et al. 2010) and a global non-hydrostatic model (NICAM; Satoh et al. 2008; Tomita and Satoh 2004) for simulating sub-seasonal boreal summer atmospheric phenomena using the high-end computing resources provided by the National Science Foundation. This particular paper aims to assess the modeling capability for simulating these phenomena in the areas of common interest.

The project will help to assess the common notion that high-resolution modeling is a promising way to improve our understanding of extreme events. In terms of TC research, "high-resolution hydrostatic models" contributed an important advancement in the projection of future change (IPCC AR4, 2007), with the Meteorological Research Institute 20-km mesh hydrostatic model being among the highest resolution available at that time (Oouchi et al. 2006). However, sufficient consensus is yet to be reached on the reliability and general efficacies of high-resolution models for TC research. Among other things, concerns have been raised over the uncertainty in the cumulus convection scheme, which was developed originally for a model with a resolution of O(100 km) (Oouchi et al. 2006). The mechanism of model-simulated TC genesis in the western North Pacific and Indian Ocean basins in association with the tropical precursor disturbance such as MJO is also unclear when compared to the observational evidence (Nakazawa 1988; Liebmann et al. 1994; Camargo et al. 2009). The Project Athena is the first opportunity to investigate high-resolution simulation (10 km for IFS and 7 km for NICAM) of the boreal summer period for multiple years. We are able to fill the gap between the previous case-study approaches and future ensemble simulations with many years of time integration.

3 Model descriptions and experimental design

We analyzed output from two types of global atmospheric models: a global non-hydrostatic grid model (NICAM), and a hydrostatic spectral model (IFS). NICAM is developed at JAMSTEC (Japan Agency for Marine-Earth Science and Technology) and the University of Tokyo (Satoh et al. 2008; Tomita and Satoh 2004). Its horizontal grid interval is approximately 7 km. There are 40 vertical levels from the surface up to 38 km and the vertical interval increases from 160 m to 2.9 km with height. We used the explicit cloud microphysics scheme of NSW6 (NICAM Single-moment Water 6: Tomita 2008), which solves for six categories of hydrometeors (water vapor, cloud water, cloud ice, rain, snow, and graupel). Turbulent closure is calculated using level 2 of the Mellow-Yamada Nakanishi-Niino scheme (MYNN2; Nakanishi and Niino 2006; Noda et al. 2010). The radiation scheme is mstrnX (Sekiguchi and Nakajima 2008). The land surface model is MATSIRO (Minimal Advanced Treatments of Surface Interaction and RunOff; Takata et al. 2003). The bulk surface flux over the ocean is calculated following Louis (1979). A single layer slab ocean model is employed. Sea surface temperature (SST) is nudged toward the observed daily $0.25° \times 0.25°$ SST, the NCEP Reynolds Optimally Interpolated (OI) SST (Reynolds et al. 2007). Sea ice mass is nudged toward the

CMIP3 model ensemble mean of the monthly sea ice mass averaged over 1979–1999. The nudging relaxation time is 5 days. No gravity wave drag is parameterized in this study. The atmospheric initial conditions for the NICAM were NCEP FNL Operational Grid Analysis ds083.2. NICAM outputs 3-hourly-snapshot data for 3D variables, and both 6-hourly snapshot and 1-hourly mean and snapshot data for 2D variables.

ECMWF has been developing the comprehensive Earth-system model IFS (http://www.ecmwf.int/research/ifsdocs/), and in this study we run the atmospheric part of the IFS. The horizontal resolution is T2047 (about 10 km) and there are 91 vertical levels whose top is approximately 0.01 hPa. The IFS run used cumulus convection based on Tiedtke (1989). For the simulation until 2001, SST and sea ice are specified from the weekly $1° \times 1°$ NCEP Reynolds OI dataset (Reynolds et al. 2002). From 2002 onward, they are specified from the daily dataset from the ECMWF operational analysis. The atmospheric initial conditions for the IFS were ERA-Interim. IFS outputs 6-hourly snapshot data for all variables. Details of the schemes and climatology of the current configuration of IFS are described by Bechtold et al. (2008) and Jung et al. (2010).

The two models were intended to run for the same periods: all the simulations started on 21 May for each year between 2001 and 2009 and run for about 100 days. For NICAM, however, the run for 2003 was not able to be executed due to model instability. Thus, we use the same 8 years of data for both NICAM and IFS.

The resolution used in this study is even higher than the range of 20–100 km that is increasingly being populated by atmospheric models utilized in climate study. Even though the motivation of this study is straightforward, the differences in model configurations must be carefully considered in this study. The behavior of these different models in terms of the ISO/MJO and TCs is interesting to be explored since the models have similar horizontal grid intervals. Firstly, the two models are based on different dynamical cores, and the horizontal resolutions are affected by their own numerical schemes. In principle, the effective resolutions (resolvable scales) of the numerical models are not the same as the grid intervals (10 km for IFS, and 7 km for NICAM), and depend on the specific method of numerical discretization (Skamarock 2004; Iga et al. 2007). Secondly, the two models have not necessarily been tested and tuned for various cases, for example, the 10 km-mesh IFS has not been used in various configurations before Project Athena. Until the present study, the longest simulation with the 7 km-mesh NICAM had been at most 3 months (Oouchi et al. 2009a, b), and Project Athena is the first opportunity to examine the statistical behavior of the ISO/MJO of NICAM using numerical data for more than a few years of simulations. Moreover, NICAM has never been used for operational purposes of numerical weather prediction (NWP), and has not been evaluated or tuned by methods used for NWP models. The striking difference between the two models is the treatment of deep cumulus convective processes: IFS uses the mass flux type cumulus parameterization (Tiedtke 1989; Bechtold et al. 2008) and NICAM explicitly calculates deep convective circulations without using cumulus parameterization. We expect that some aspects of the numerical results result from the different treatment of the cumulus processes.

4 ISO events in the Indian Ocean

First, we show a brief description of the climatological fields simulated by both models. Figure 1 shows the 8-year averaged zonal wind field at 850 hPa over the warm pool region. The Somali jet, a well-known characteristic of the boreal summer monsoon circulation which forms a part of the Asian summer monsoon circulation in the western Indian Ocean, is pronounced during the three-month simulation period. Westerlies prevail along $10°–15°N$, and extend eastward associated with the evolution of the monsoon (ERA Interim, bottom panels). The horizontal pattern and the seasonal march of the monsoon are well reproduced by IFS, albeit with over-prediction of the magnitude of the westerlies (middle panels). In contrast, NICAM fails to reproduce the eastward migration of westerlies and under-predicts the Somali jet (top panels). Figure 2 show time-latitude plots of the 8-year averaged $60°–90°E$ mean zonal wind at 850 hPa and surface precipitation. The peaks of the westerlies and precipitation are located at $5°–10°N$ during May, shift northward in early June, and stay around $15°–20°N$ through June to August (bottom panel). Both simulations capture the intensification and northward displacement of maximum westerly winds and precipitation in early June except for some biases in the excessive peak intensity ($\sim 15°N$) in IFS, and insufficient intensity and peak latitudes occurring 5–10 degrees northward in NICAM. The discrepancies described above are relatively small in the first month of simulation.

Of a number of indices for monitoring the Asian summer monsoon (e.g., Webster and Yang 1992; Parthasarathy et al. 1994; Kawamura 1998; Goswami et al. 1999; Wang and Fan 1999; Wang et al. 2001), we use the Indian Monsoon Index (IMI) to see how the seasonal march and intra-seasonal oscillations are simulated. IMI is defined by the magnitude of easterly shear at 850 hPa (Wang et al. 2001), namely, the difference between the average zonal wind over the domains of ($40°–80°E$, $5°–15°N$) and ($70°–90°E$, $20°–30°N$), and is shown in Fig. 3. The 8-year averaged IMI (Fig. 3a) in ERA Interim gradually increases from April (less than -2) to June (3–9), changes sign
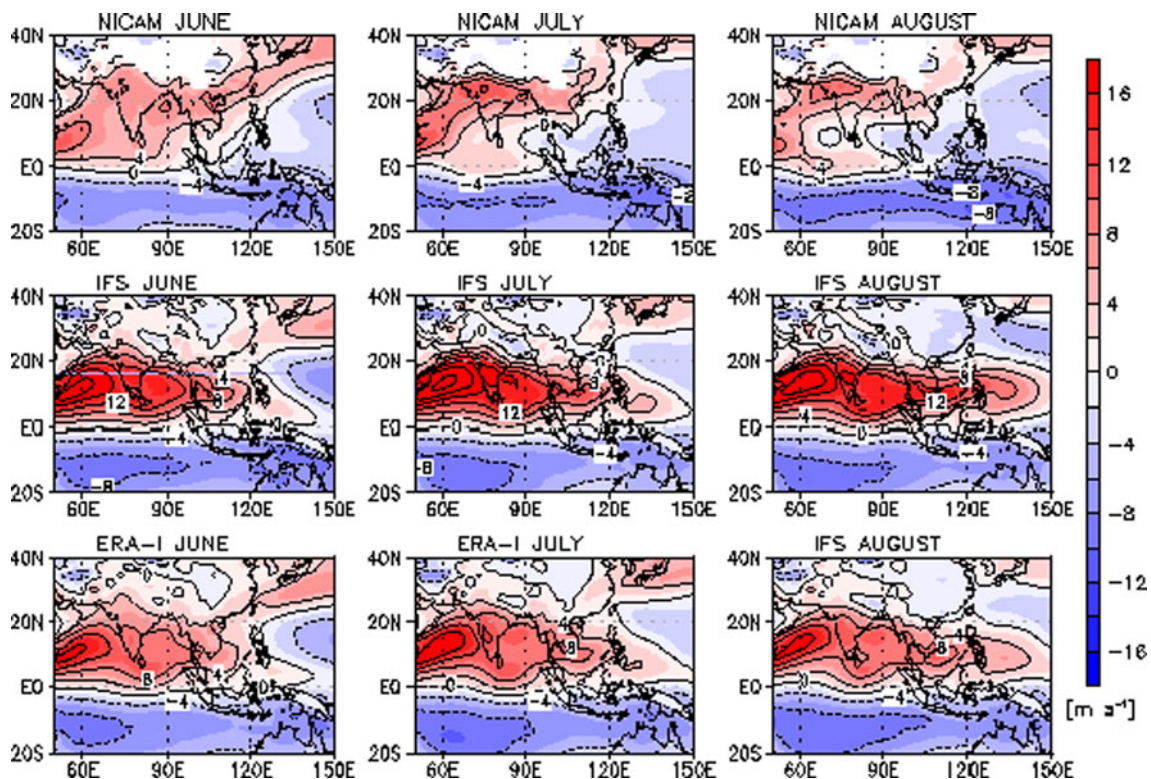
Fig. 1 The 8-year averaged monthly mean zonal wind at 850 hPa in NICAM (*top*) and IFS (*middle*) simulations in comparison with ERA-Interim (*bottom*)
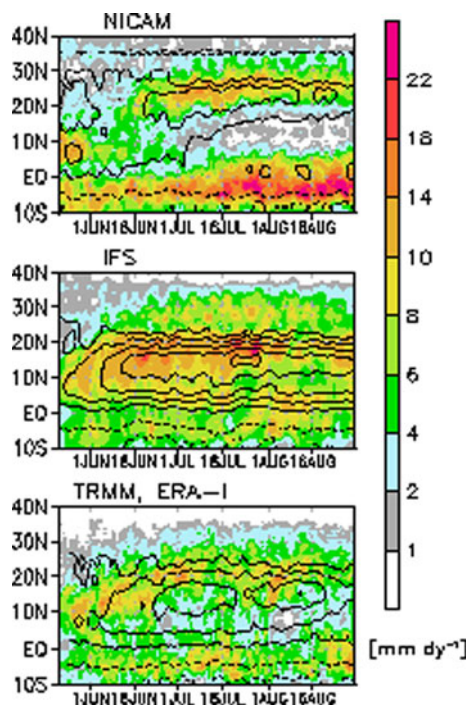

Fig. 2 Time-latitude sections of the 8-year 60°–90°E averaged precipitation (*color*) and zonal wind at 850 hPa (*contour lines*) in NICAM (*top*) and IFS (*middle*) simulations in comparison with TRMM-3B42 and ERA-Interim and (*bottom*). Contour intervals for zonal wind are 4 m s^{-1} (*solid*: positive, *broken*: negative). Zero contour lines are omitted

around 21 May, and is positive (6–9) in the following 2 months (cf. the climatological 'onset' date of the summer Indian monsoon is 1 June; Flatau et al. 2001). NICAM fails to reproduce the gradual rise of IMI (seasonal march), as expected from Fig. 1. On average, IFS (NICAM) over-predicts (underpredicts) meridional shear of zonal winds associated with monsoon circulation. We did not identify causes of the biases, but they are affected by changes in cloud processes and land and ocean surface conditions.

Figure 3b–i shows anomalous IMI from the 8-year average for each simulated year. Fluctuations with time scales of 2–4 weeks, which are referred to as intra-seasonal oscillations (ISO), are evident in all years in ERA Interim. ISOs are masked out by the 8-year average (Fig. 3a) because the timing of the ISOs are not exactly the same in every year. However, it is noteworthy that the monsoon onset is often triggered by an ISO event (Lau and Chan 1986; Annamalai and Slingo 2001). Correlation coefficients of the time series of IMI between simulations and ERA-Interim (Fig. 3) for the first, second, and third month of integration for each year are summarized in Table 1. NICAM reproduce the ISO in the first month of simulation better than in the latter 2 months, with correlation coefficients exceeding 0.8 in some years (e.g., 2002, 2006 and 2009), although statistical significance are not necessarily guaranteed by the eight samples. In the IFS simulations

Fig. 3 Time series of the Indian Monsoon Index (Wang et al. 2001) for NICAM and IFS simulations and ERA-Interim data. **a** The 8-year average and **b–i** anomaly from the average are plotted. 5-day running mean is operated
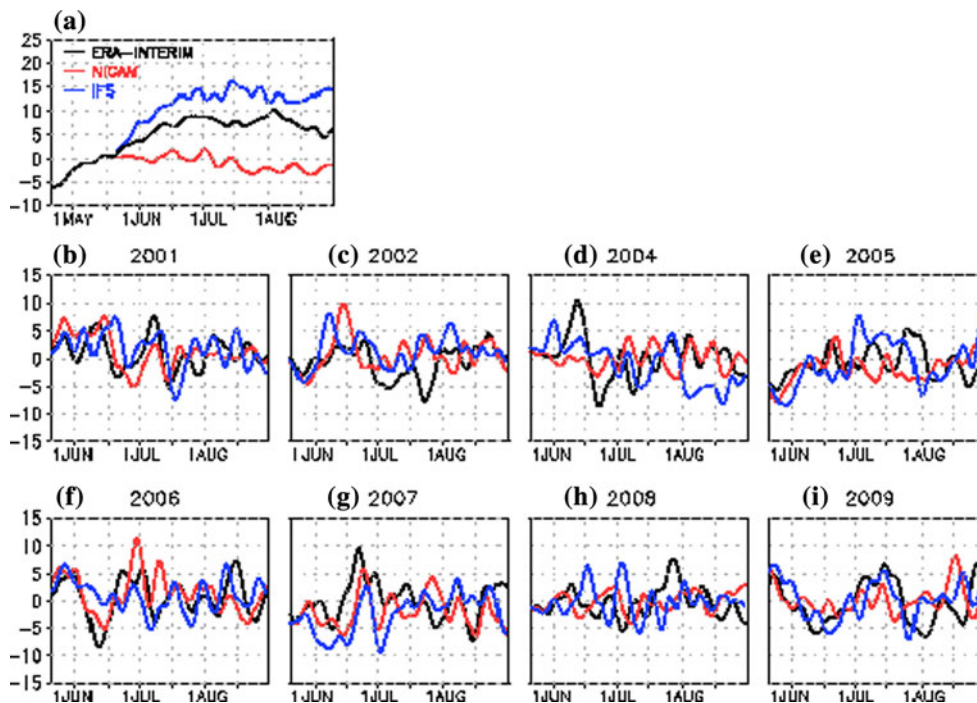

Table 1 Correlation coefficients of the time series of anomalous IMI (Fig. 3b–i) in NICAM and IFS simulations against that in ERA-Interim for the 1st, 2nd, and 3rd month of simulation period

Year	NICAM			IFS		
	1st	2nd	3rd	1st	2nd	3rd
2001	0.730	0.663	−0.287	−0.515	0.467	−0.138
2002	0.879	−0.145	−0.546	0.531	0.673	−0.058
2004	0.384	0.304	0.063	0.163	−0.572	0.093
2005	0.877	−0.322	−0.655	0.493	0.044	0.263
2006	0.911	0.006	−0.081	0.653	0.402	0.393
2007	0.269	0.404	0.242	0.201	0.248	0.672
2008	0.294	0.137	−0.141	−0.226	−0.688	−0.095
2009	0.847	0.510	−0.205	0.836	0.712	0.152
Average	0.648	0.194	−0.201	0.267	0.160	0.160
SD	0.264	0.315	0.277	0.427	0.499	0.258

8-year averages and standard deviation are also presented for the three periods

coefficients in the first and second month are equivalent and decreasing in the third month.

In the remainder of this section, we discuss the reproducibility of the simulated ISO associated with Indian monsoon onset. Not only the evolution of monsoon onset (seasonal change) but also the ISOs in the Indian monsoon region are characterized by northward migration of westerlies and convection (Yasunari 1979, 1980; Sikka and Gadgil 1980; Wang and Rui 1990). Figure 4 presents the time-latitude plots of 60°–90°E averaged zonal wind at 850 hPa and surface precipitation (anomaly from the

8-year average; Fig. 2. NICAM and IFS simulations are compared with ERA Interim and Tropical Rainfall Measurement Mission, TRMM-3B42 datasets for the first 52 days of simulation. Northward propagation of the westerly anomaly preceded by a peak in precipitation on an intra-seasonal time scale is observed during late May to early June in every year. The time-lag between the peaks of westerlies and precipitation is due to enhanced precipitation at the front edge of the westerlies. The timing of the northward propagation of the maximum westerly anomaly from lower latitudes (0°–5°N) to around 20°N coincides with the increase of IMI (Fig. 2). The intensification of the westerly anomaly as well as the precipitation events is seen throughout the northward migration (i.e., 0°–5°N to around 20°N) (Fig. 4, bottom panels). NICAM and IFS simulations capture the latitudinal movement of these events in 2001, 2002, 2005, 2006, and 2009 (Fig. 3 top and bottom panels), although the magnitude and timing of each of the events are not realistically reproduced. In the IFS simulations, the fluctuations between 10° and 15°N are rather pronounced than in ERA Interim and in NICAM simulations. Among the 8-year samples, the 2006 events are clearly defined in observations and simulations.

Figure 5 shows horizontal distributions of pentad-mean precipitation over the warm pool region during the northward propagation event in 2006 (Fig. 4). The bottom panels show those of TRMM-3B42. Precipitation becomes active between 60° and 90°E around the equator from 15 to 19 June (Fig. 5a), and the precipitation region extends northward and eastward, and forms a NW–SE tilted banded
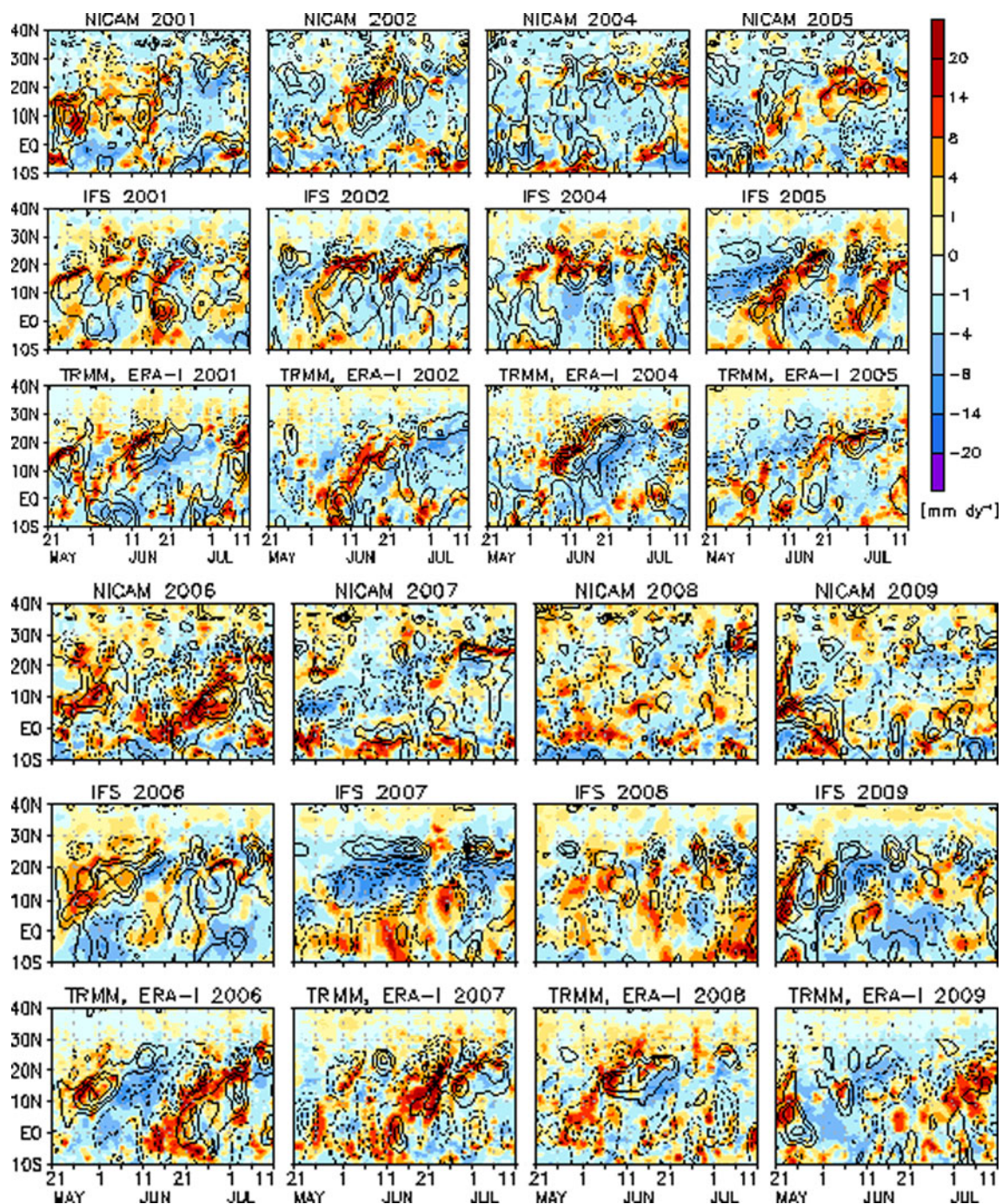
Fig. 4 Time-latitude sections of anomalous 60°–90°E average surface precipitation (*color*) and zonal wind at 850 hPa (*contour lines*) in the initial 52 days of NICAM (*top*) and IFS (*middle*) simulations in comparison 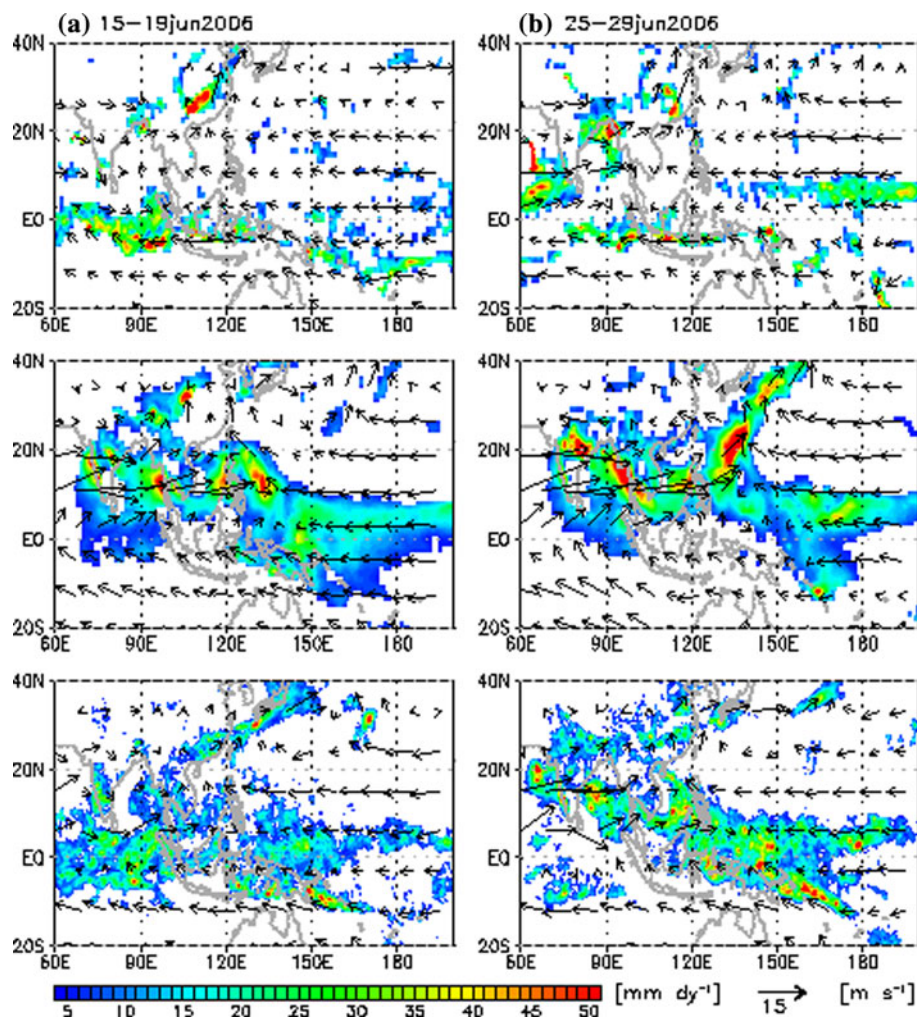with TRMM-3B42 and ERA-Interim data (*bottom*). The anomalies from the 8-year average (Fig. 2) are plotted. Contour intervals for zonal wind are 2 m s^{-1} (*solid*: positive, *broken*: negative). Zero contour lines are omitted

structure over 90°–180°E from 25 to 29 June (Fig. 5b). Such a banded configuration is typical of precipitation in this season, and the location and strength of the rainband varies on an intra-seasonal time scale (Yasunari 1979, 1980; Sikka and Gadgil 1980; Lau and Chan 1986; Wang and Rui 1990; Annamalai and Slingo 2001; Kemball-Cook and Wang 2001; Waliser et al. 2003). Mesoscale regions of intense precipitation appear over the northeast Arabian Sea and Bay of Bengal (Fig. 5b).

The configuration of the large-scale rainband is well reproduced by IFS (the middle panels in Fig. 5). Although NICAM does not adequately reproduce this rainband

Fig. 5 Pentad-mean precipitation and wind vectors at 850 hPa for **a** 15–19 and **b** 25–29 June 2006 for NICAM (*top*) and IFS (*middle*) simulations in comparison with TRMM-3B42 and ERA-Interim data (*bottom*)

structure, the formation and temporal variation of the mesoscale heavy precipitation, as found by the northeastward movement in 60°–90°E and eastward shift along the Equator, are better simulated by NICAM (the top panels in Fig. 5). The bifurcation of intense precipitation (i.e., northward and eastward movement, as discussed by Lau and Chan 1986; Wang and Rui 1990; Annamalai and Slingo 2001, and others) after 20 June is well reproduced by NICAM, although the timing of mesoscale heavy precipitation lags that in TRMM 3B42. The biases of persistent precipitation along 0°–5°S and suppressed convection in the western Pacific are consistent with those in Fig. 1. These results suggest that some regional mesoscale mechanisms can also control the organization of convection over the Indian monsoon region, in addition to larger-scale control associated with the monsoon system. The results of IFS are markedly different from those of NICAM, with broad distribution of moderate precipitation which generally matches the observed precipitation pattern. The mesoscale regions of heavy precipitation mostly appear along the persistent westerly belt (10°–20°N), and

northward/northeastward movement is not clear (the middle panels in Fig. 5). Such differences may be attributed to the different treatment of moist convection between the two models. The mesoscale organization of convection in the ISO events will be investigated using these high-resolution simulation results in the forthcoming studies.

5 Characteristics of MJO

In this section, the statistical behavior of the simulated ISO is analyzed by focusing on convective anomalies associated with MJO. The phase propagation and frequency of MJO are examined for both NICAM and IFS.

We use the velocity potential as a measure of convective activity of MJO, specifically the temporal evolution of meridionally averaged velocity potential anomaly from climatology ($m^2\ s^{-1}$) at 200 hPa over 10°N–10°S during the period of 21 May to 30 August. The anomalies of velocity potential are derived from the models and the observational climatologies defined by the 8-year average
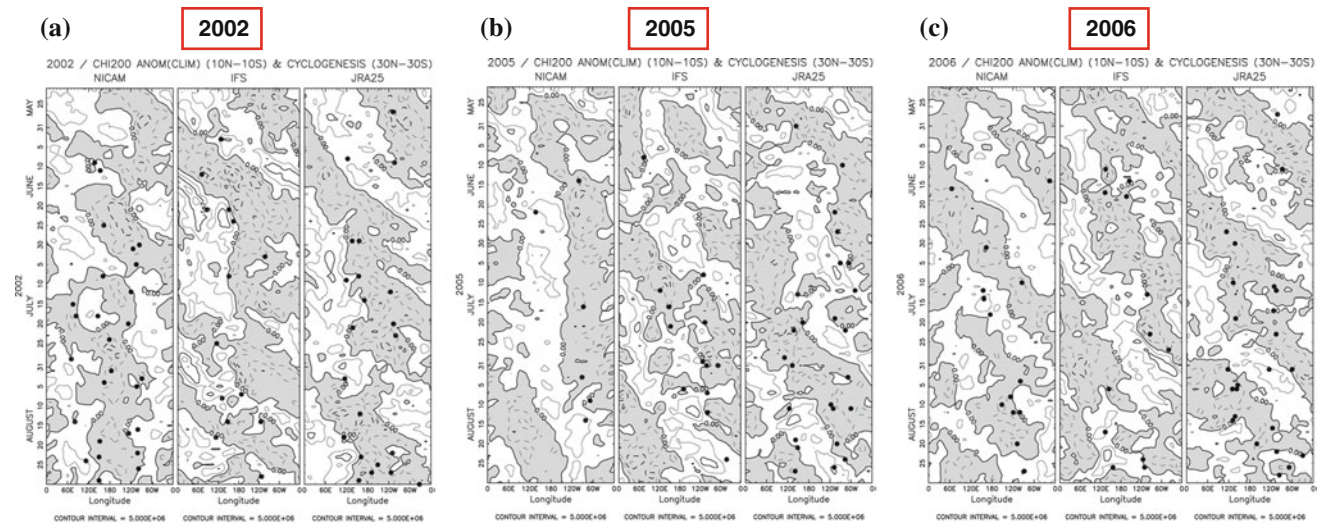
Fig. 6 Temporal evolution of meridionally-averaged velocity potential anomaly from climatology (m^2 s^{-1}) at 200 hPa over 10°N–10°S during 21 May–30 August **a** 2002, **b** 2005, and **c** 2006. The *left*, *center*, and *right* column of each panel show the results of the NICAM and IFS simulations, and the observations (re-analysis) by JRA/JCDAS analysis, respectively. The date of each panel begins at the top of each panel. Contour interval is 5.0×10^6 (m^2 s^{-1}). *Shading* (negative values) corresponds to a region of divergence. Also plotted are the locations of simulated (*left* and *center* column) and observed (*right* column) TC genesis in the latitudinal range of 30°N–30°S by *solid circles* in each panel

of daily data from the simulations and the observations from 2001 to 2009 (except 2003), respectively. The observational climatology data are derived from JRA/JCDAS (Japanese ReAnalysis/Japan Meteorological Agency Climate Data Assimilation System; Onogi et al. 2007) dataset.

Figure 6 shows the propagation of convective anomalies associated with the model-simulated and the observed MJO for the years 2002, 2005, and 2006, together with the location and timing of tropical cyclogenesis (dots). The detection method and characteristics of tropical cyclones will be described in the next section. Figure 6 shows a distinct eastward propagation of the convective anomaly, which can be observed from around 180°E during the period between 21 May and 30 August 2002 (Fig. 6a) and from the Indian Ocean during the period between 21 May and 25 August 2006 (Fig. 6c). On the other hand, in Fig. 6b (2005), while the MJO-related eastward propagation during May and early June is relatively faster than the MJO timescale, the 45 days of eastward propagation during July 15 to August 30 is not. As shown later in Figs. 7h and 8h, MJO was inactive during the period from May to early June 2005. From all the results of the 8-year simulations, IFS well reproduced the convective anomaly in 2002 and 2007, while NICAM did so in 2006 and 2009 (figures not shown).

In order to capture the MJO signal quantitatively, empirical orthogonal function (EOF) analysis (Taniguchi et al. 2010) of the 30-day low-pass filtered velocity potential anomaly at 200 hPa was performed for the period between 21 May and 31 July in each year. The period of data used for the EOF analysis was restricted to the first 72 days of data in each year, because the last 30 days fell out of the analysis period due to the application of a low-pass filter. The data for low-pass filtering was constructed by appending observational data for the 21 April to 20 May to the original simulation data, to avoid loss of the first 30 days of simulation data. The eigenfunctions and associated eigenvalues (scores) of the EOF1 and EOF2 modes are shown in Figs. 7 and 8 for the same years as in Fig. 6, respectively. In the MJO-active period, the zonal wavenumber-1 component was dominant in both EOF1 and EOF2 modes in 2002 (Fig. 7g) and 2006 (Fig. 7i), which had active convective regions associated with the MJO over the maritime continent or the Indian Ocean as is well known from observations. The corresponding simulated results of IFS and NICAM also captured these features, as shown in Fig. 7c, d, respectively. The simulated phase propagations of the MJO for IFS in 2002 and NICAM in 2006 reproduce the characteristics of the observations (IFS: Fig. 8d vs. g; NICAM: Fig. 8c vs. i). On the other hand, for cases in which the eastward propagation of the convective anomaly was not captured in Fig. 6, the eigenmodes of EOF1 and EOF2 have a different structure (Fig. 7a, f). For the MJO-inactive case in 2005, the leading modes of EOF1 and EOF2 in the observations have zonal wavenumber-2 components, and these modes are well captured by both NICAM and IFS (Fig. 7b, e, h). All time series of the
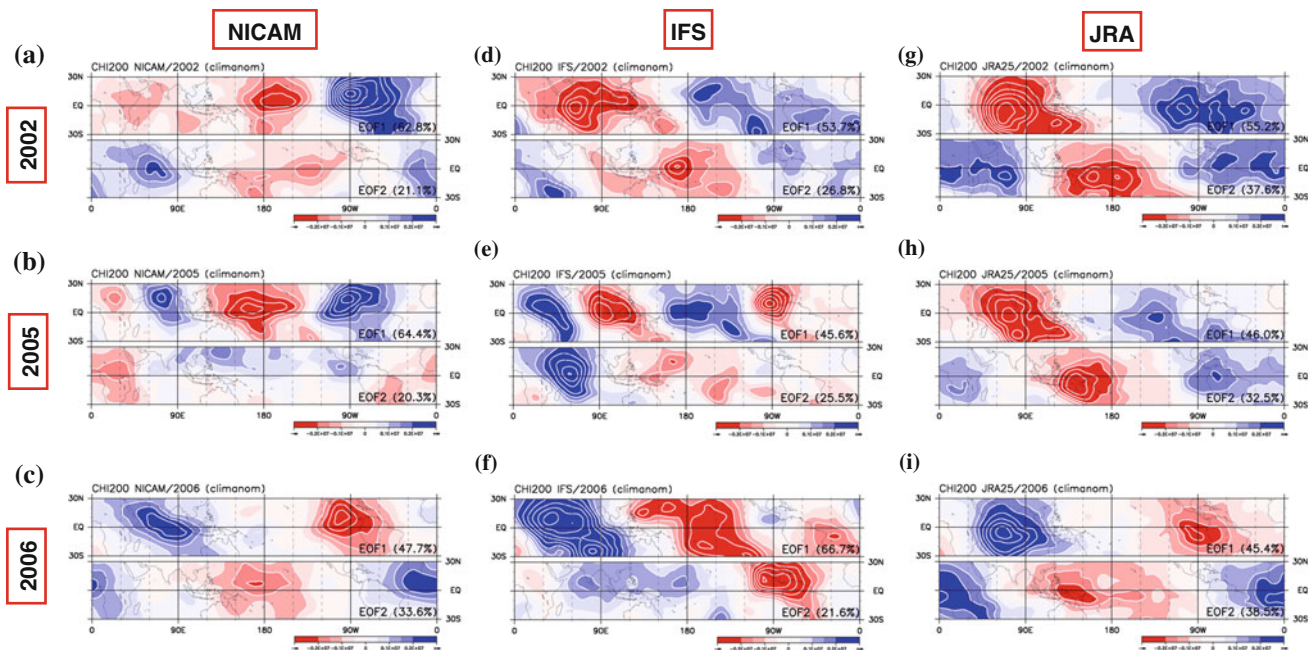
Fig. 7 Empirical orthogonal function (EOF) analysis of 30-day low-pass filtered velocity potential anomaly from climatology (m² s⁻¹) at 200 hPa during 21 May–31 July 2002 (top 3 panels; **a**, **d**, and **g**), 2005 (middle 3 panels; **b**, **e**, and **h**), and 2006 (bottom 3 panels; **c**, **f**, and **i**). The *left* (**a–c**), *center* (**d–f**), and *right* (**g–i**) columns show the result of the NICAM and IFS simulations, and the observations (re-analysis) by JRA/JCDAS analysis, respectively. The *upper* and *lower* figures of each panel show the eigenmodes of EOF1 and EOF2, respectively. The *red* and *blue* end of the spectrum indicate the region of divergence and convergence of velocity field, respectively. Contour interval is 0.5 × 10⁶ (m² s⁻¹). Contribution rate of each eigenmode against the total variance is shown at the lower right of each figure

corresponding modes of EOF1 and EOF2 in 2005 (Fig. 7b, e, h) have small amplitude from the center of origin, and indicate weak MJO (Fig. 8b, e, h).

As shown above, the performance in simulating MJO varies from year to year in both models. To show global statistics of MJO and equatorial disturbances, Fig. 9 designates the zonal wavenumber-frequency power spectra (Wheeler and Kiladis 1999) of the symmetric component of the velocity potential anomaly, which is calculated by averaging each spectrum from 21 May to 30 August in each year. The original and background power spectra are consistently simulated (Fig. 9a, d and b, e) compared to the observations (Fig. 9g, h). The ratios of the background power to the original power indicate differences among NICAM (Fig. 9c), IFS (Fig. 9f) and observations (Fig. 9i). One such difference is the reproducibility of the MJO signal. A distinct signal of the MJO can be seen in the zonal wavenumber 1 with a period around 45 days in the NICAM results (Fig. 9c) and the observations (Fig. 9i), while the corresponding signal in IFS has a shorter period (Fig. 9f). It is of note, however, that an analysis without the first 11 days each year shows that IFS has a sizable power in the equatorial Kelvin wave and MJO at zonal wavenumber 1. The peak period of MJO resides around 45-day and significant power extends to 60-day as consistent with Jung et al. (2010), which is comparable to that of

observation and NICAM. Therefore, the assessment of the model-inherent spectral power needs careful interpretation that varies with data sampling period being susceptible to initial conditions. A strong signal of equatorial Kelvin waves is detected around with a period of less than 15 days in the substantial range of zonal wavenumbers greater than 1 in NICAM and the observations, while this signal is relatively weak in IFS.

6 Statistical behavior of tropical cyclones

In this section, we examine the statistical behavior of the simulated TC with a focus on the season-long synthesis of track, frequency and intensity. Manganello et al. (2011) have analyzed the TC behavior in longer runs of the IFS at T2047 resolution, in comparison with other, lower resolution versions of IFS. Here we examine only the June–August runs for 8 years done commonly with IFS at T2047 and with NICAM. The tracking method used here almost follows that of Oouchi et al. (2006). TC frequency is quite sensitive to the maximum wind speed threshold (traced at the 10-m height), and it needs to be considered carefully. Walsh et al. (2007) suggest that this threshold depends on horizontal resolution of models, and it is appreciate to use 17.5 m s⁻¹ as the threshold for around 10-km mesh model
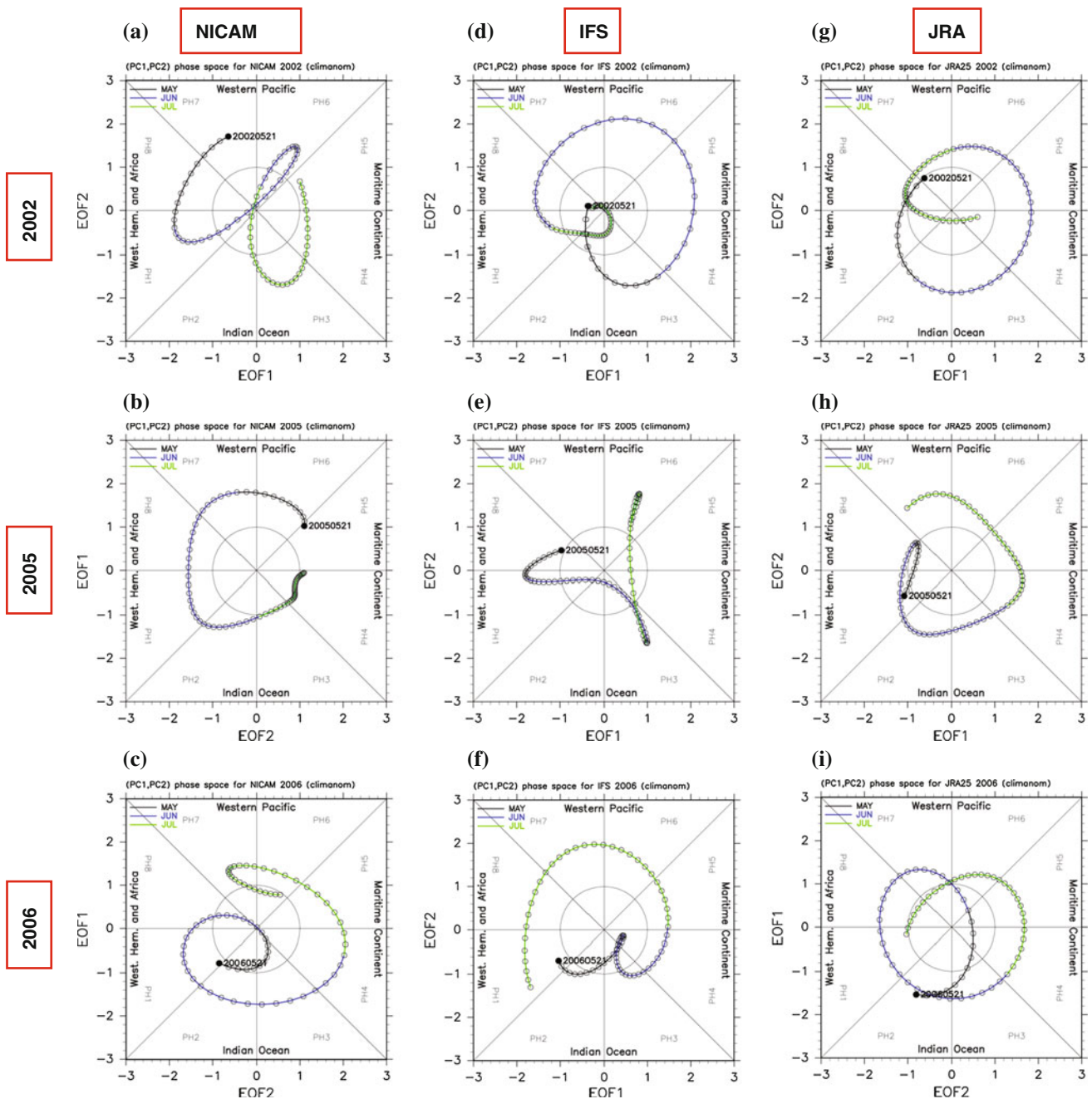
Fig. 8 Time series of corresponding EOF1 and EOF2 modes of the plots in Fig. 7 in phase space. *Black*, *blue*, and *green cascading lines with open circles* show the trajectories from 21 May to 31 July 2002 (**a**, **d**, and **g**), 2005 (**b**, **e**, and **h**), and 2006 (**c**, **f**, and **i**), respectively. The *solid circles* indicate the score of 21 May in each year. The *left* (**a–c**), *center* (**d–f**), and *right* (**g–i**) columns show the time series of scores obtained by the EOF analysis of the NICAM and IFS simulations, and the observations (re-analysis) by JRA/JCDAS analysis, respectively. The eight equal-angle phase-space categories are defined after Wheeler and Hendon (2004). The *x* and *y* axes in each figure are defined by the structure of the eigenmode of EOF1 and EOF2 shown by Fig. 7

following their suggestion. In this study, therefore, the threshold is 17.5 m s^{-1} for NICAM. However, that of IFS is 15.4 m s^{-1}, because the numerical integration time step is different between the two models (0.5 min for NICAM and 7.5 min for IFS), and a conversion between the different time sampling periods may be required for comparison. We applied a conversion ratio of 0.88, which is used for a threshold assessment in an operational procedure of tropical cyclone data processing (Knaff et al. 2010), and use a threshold of 15.4 m s^{-1} for IFS. The best track dataset from IBTrACS (v03r01) is employed for verification (http://www.ncdc.noaa.gov/oa/ibtracs/).
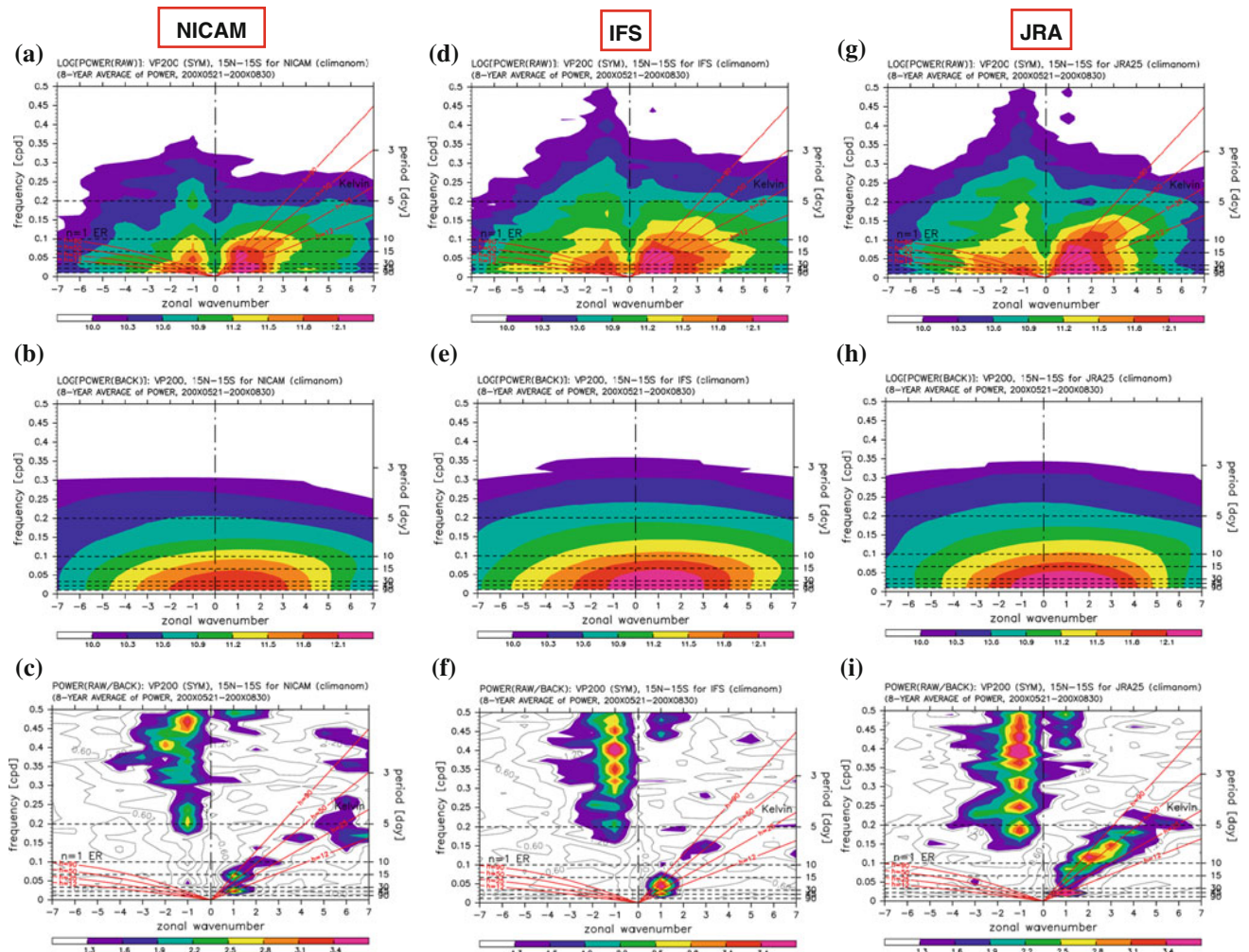
Fig. 9 Zonal wavenumber-frequency power spectra of the symmetric component of the velocity potential anomaly, calculated by averaging each spectrum from 21 May to 30 August 2001 to 2009 except 2003. The *top* (**a**, **d**, and **g**), *middle* (**b**, **e**, and **h**), and *bottom* (**c**, **f**, and **i**) rows indicate the original power spectra, the background power spectra, and the ratio of the original power divided by the background power, respectively, while the *left* (**a**–**c**), *center* (**d**–**f**), and *right* (**g**–**i**) columns show the results of the NICAM and IFS simulations, and the observations (re-analysis) by JRA/JCDAS analysis, respectively. For the components of the original power spectrum (**a**, **d**, and **g**), the power was calculated for seven successive overlapping 96-day segments of 102 days in each year, and summed over 15°N–15°S, and the base-10 logarithm taken for plotting, which corresponds to Fig. 1 of Wheeler and Kiladis (1999, hereafter WK99). Shading is plotted only over a power of 10.0. For the components of the background power spectrum (**b**, **e**, and **h**), each power has been calculated by averaging each individual original power spectra of Fig. 9a, d, g, and smoothing many times with a 1-2-1 filter in both wavenumber and frequency, which corresponds to Fig. 2 of WK99. Shading is the same as the original power spectra. For the components of the ratio of the original power divided by the background power (**c**, **f**, and **i**); which corresponds to Fig. 3b of WK99), the contour interval is 0.3, and shading begins at a value of 1.3 for which the spectral signatures are statistically significantly above the background at the 95% level (based on 121 degree of freedom). Superimposed are the dispersion curves of the odd meridional mode-numbered equatorial waves for the three equivalent depths of $h = 12, 25, 50$ and 90 m in the figures of **a**, **d**, **g**, **c**, **f**, and **i**. Frequency spectral bandwidth is 1/96 cpd

Figure 10 shows the cyclogenesis density (number of TC detected in 5-degree lat/lon intervals per year) distribution for June-July–August (JJA). The cyclogenesis location is defined as where the wind speed of a given TC exceeds the wind speed threshold for the first time. The cyclogenesis density is high over the western and eastern Pacific in the best track data (a), and NICAM (b) and IFS (c) also capture this trend. Both models underestimate the occurrence of tropical cyclogenesis compared to the best track data, especially over the Gulf of Mexico and the Caribbean Sea. Over the Indian Ocean, both models produce more TCs than observed. NICAM simulates TCs even near the equatorial region and IFS simulates more TCs than the best track data over the Bay of Bengal. Overall the IFS better simulates the TC density, even over the East Pacific where NICAM overestimates. Focusing on the NICAM
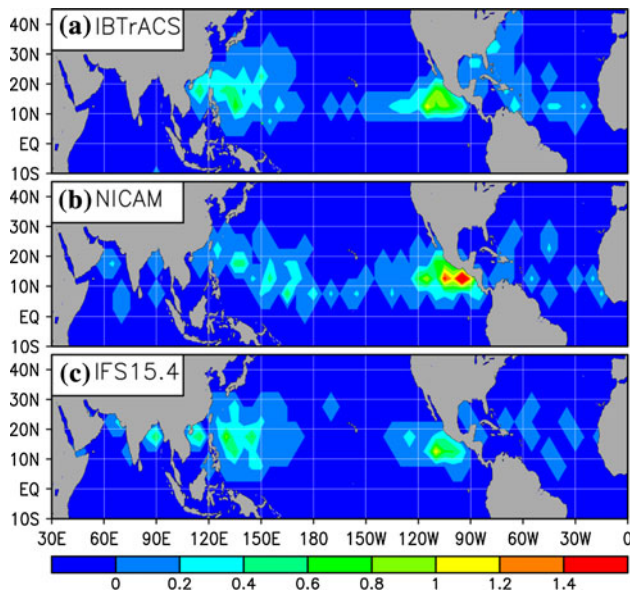
Fig. 10 Cyclogenesis density (number per 5° lat.-long. area per year) distribution in June–August in **a** the observations (IBTrACS), **b** NICAM, and **c** IFS

Table 2 Cyclogenesis frequency per model, month and ocean basin, where the Indian Ocean is defined from 30° to 100°E, the western Pacific from 100° to 180°E, the eastern Pacific from 180° to 90°W and the Atlantic from 90° to 30°E

Case	Indian O.	W. Pacific	E. Pacific	Atlantic	Global
IBTrACs/ JJA	2	78	69	39	188
June	1	12	7	1	21
July	1	25	27	10	63
August	0	41	35	28	104
NICAM/JJA	8	42	111	25	196
June	5	22	21	8	56
July	1	19	45	5	70
August	2	11	45	12	70
IFS 17.5/JJA	9	58	31	10	108
June	4	9	8	1	22
July	3	21	13	5	42
August	2	28	10	4	44
IFS 15.4/JJA	15	74	45	11	145
June	5	10	13	1	29
July	6	29	15	5	55
August	4	35	17	5	61

simulation, the density over the eastern Pacific appears closer to the best track data than over the western Pacific, where the higher density area is located more eastward than observations; there were void of TCs over the South China Sea, west of the western Pacific in NICAM. The high density of TC in NICAM corresponds to the excessive precipitation bias over the equatorial Indian Ocean as discussed in Oouchi et al. (2009b).

The total number of TCs in the respective ocean basins and months is shown in Table 2. The definition of the ocean basins follows that of Yamada et al. (2010). Over the western and eastern Pacific and the Atlantic, observed TCs increase from June to August. This increase is mainly associated with the seasonal migration of the western Pacific monsoon trough in the observations (Yokoi et al. 2009). NICAM simulates no appreciable increase of TCs from July to August. This can be explained by a few climatological factors, one of which is as follows. Figure 1 indicates that NICAM fails to reproduce the eastward extension of the westerly zonal wind that is strong around 10°N in the observations. The extension is pivotal in providing synoptic-scale cyclonic circulation that is conducive to TC formation and development in the western part of the western Pacific. The lack of this feature in NICAM is likely responsible for the small number of TCs in August. On the other hand, IFS captures the eastward extension of the westerly region well, although the westerly zonal wind is stronger than observed. Nonetheless, the seasonal monotonic increase in TC frequency is absent from June to August in the IFS results. An additional analysis revealed that IFS tends to create larger-than-observed vertical wind

shear in this region that inhibits cyclogenesis toward August (not shown). Over the eastern Pacific, NICAM captures the seasonal increase of cyclogenesis better than IFS.

Table 2 also suggests that cyclogenesis frequency is sensitive to the wind speed threshold. Using a threshold of 17.5 m s^{-1}, the frequency in IFS is less than that of the observations and the NICAM simulation, while it is almost comparable to NICAM with a threshold of 15.4 m s^{-1}. The frequency difference due to a different threshold is quite significant (more than double) over the the Indian Ocean, eastern and western Pacific, which suggests that relatively weaker or shorter-lived TCs are more frequent over these basins than in the western Pacific in the IFS simulation.

The TC tracks are shown in Fig. 11. The tracks simulated in the models for the respective ocean basins are mainly consistent with the observations; however, some discrepancies are apparent. NICAM simulates a substantial number of TCs that originate over the central and eastern Pacific and travel across the date line compared to the observations. Some of them are longer-lived than observed and travel over a longer distance than observed (e.g., TCs in 2004). The reason for such TC features in NICAM is likely to be associated with the somewhat weaker vertical shear over the central Pacific region compared to observations (not shown). On the other hand, TC in IFS does not move in such a long distance in most of the basins; rather, TCs are less frequent than observed as shown in Table 2.

Fig. 11 TC tracks in June to August of each year. *Black line*: best track from IBTrACS, *red line*: NICAM simulation, *blue line*: IFS simulation
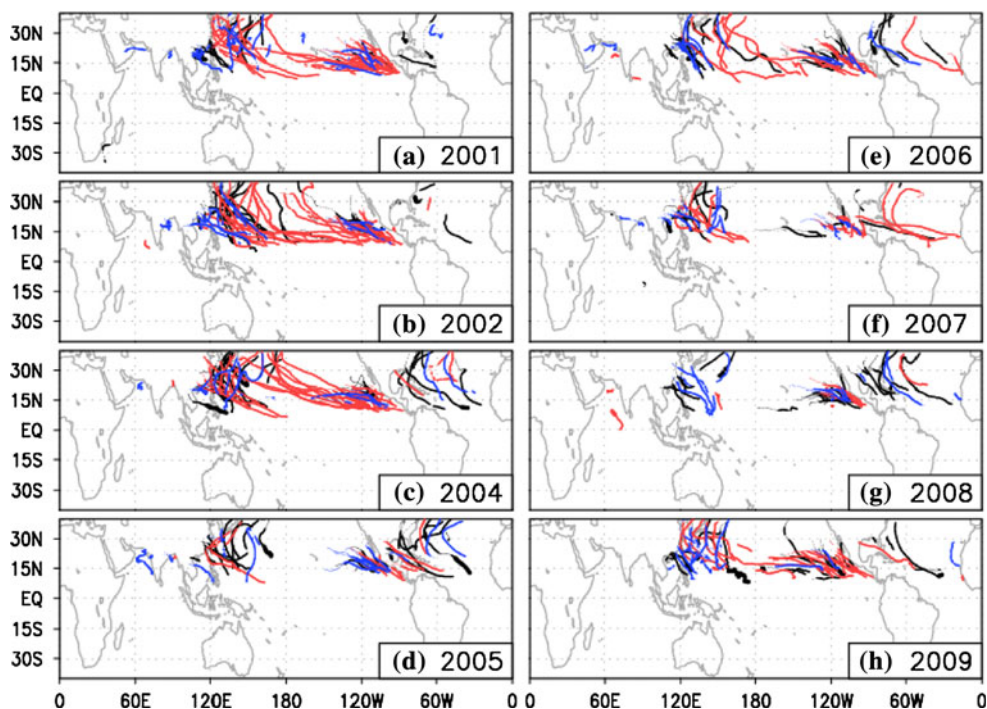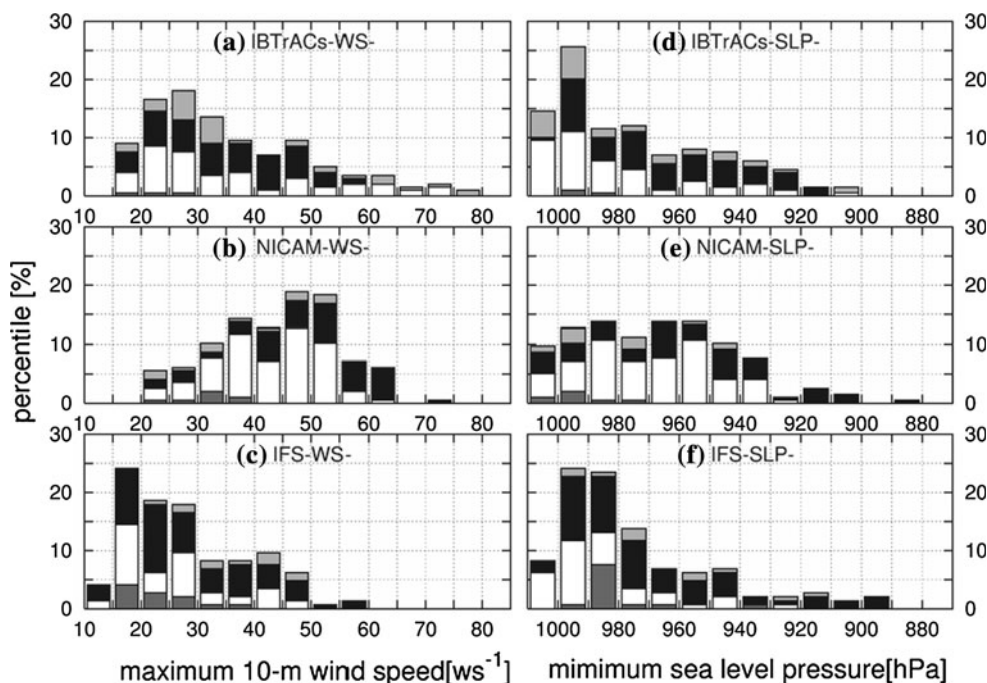

Fig. 12 Rank histograms of TCs intensity: the maximum attained 10-m wind speed (m s^{-1}) and the minimum sea level pressure (hPa) for their life-cycle in **a**, **d** the observations (IBTrACs), **b**, **e** NICAM, and **c**, **f** IFS respectively. The *Gray*, *white*, *black* and *light gray boxes* indicate percentages in the Indian Ocean, Western Pacific, Eastern Pacific and Atlantic, respectively. Note that the integration time step is different between the two models (0.5 min for NICAM and 7.5 min for IFS)

In order to examine TC intensity, Fig. 12 shows histograms of the maximum attained 10-m wind speed (MWS) and the minimum sea level pressure (MSLP) for all TCs. We should note that the difference between time steps are used for the two models (0.5 min for NICAM and 7.5 min for IFS). We may need to interpret that wind speeds of the snapshot data of NICAM and IFS represent different time averaged data, such as 1 and 10 min average winds,

respectively. The IBTrACs data of Fig. 12a (upper left panel) use both 1 and 10 min average for MWS. In terms of MWS, the observations (upper left panel) reveal two peaks between 25 and 30 m s^{-1}, and 45 and 50 m s^{-1}. Likewise, MSLP has two peaks between 1,000 and 990 hPa, and 960 and 950 hPa (upper right panel). The IFS simulation also has two peaks (bottom panels), and NICAM simulation also has two peaks, but they are not clear. (middle panels)
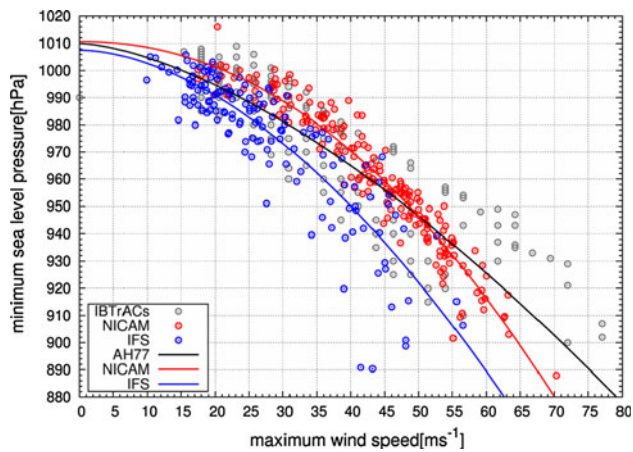
Fig. 13 Relationships between the minimum sea level pressure (MSLP) (hPa) and the maximum 10-m wind speed (MWS) (m s^{-1}) when a tropical cyclone has MSLP in the observations, IFS and NICAM simulations. Black solid line indicates the empirical relationship between MSLP and MWS (Atkinson and Holliday 1977). The datasets used are the same as Fig. 12d–f

for both MWS and MSLP. The peaks in NICAM are in the range of 45–50 m s^{-1} for MWS and 960–950 hPa for MSLP, suggesting that stronger TCs are more frequent than in the observations and IFS. Another interesting aspect of Fig. 13 is that the great majority of intense TCs (e.g., MWS exceeding 55 m s^{-1} and MSLP lower than 930 hPa) occur over the eastern Pacific in both models, which is not the case in the observations.

Analysis of the relationship between MSLP and MWS provides a way to assess intensity and the associated horizontal structure of dynamical features of the simulated TCs. Figure 13 presents scatter plots of both variables for all TCs simulated in both models and observations (Atkinson and Holliday 1977; AH77). Comparison between the simulated and observations (AH77) plots reveal that MWS is underestimated relative to MSLP for intense TC (MSLP lower than 940 hPa) in both models. This characteristic is less pronounced in NICAM than in IFS. As the observed relationship of these variables remains controversial and needs reexamination (Knaff et al. 2010), more rigorous discussion of this aspect is desirable in a future study.

7 Relationships between MJO and tropical cyclones

As a final analysis, we examine how the two models simulate the relationship between MJO and TCs. Figure 14 shows composite 200 hPa velocity potential anomalies for each MJO phase during the period of May 21 to July 31 shown by Fig. 8 but for the MJO-active period, which is defined using the same method as Taniguchi et al. (2010).

The distinct eastward propagation of convective anomalies associated with MJO is evident in all panels (Fig. 14a–c). For NICAM (Fig. 14a), the area of convective anomalies in phases 3, 4, and 5 (active convection over the Indian Ocean to the maritime continent) is larger than in the observations (Fig. 14c), while in the area in phases 2 and 7 (active convection over the Atlantic Ocean) is smaller than that in the observations. Presumably, these features are related to more active/inactive convection in NICAM compared to the observations over the regions of the Indian Ocean to the maritime continent/Atlantic Ocean, respectively. On the other hand, for IFS (Fig. 14b), the area of convective anomalies in phases 1, 2, 7, and 8 is smaller in the region of the Atlantic Ocean to the African continent than that of the observations. This is probably due to inactive convection in IFS compared to the observations in the western hemisphere. The locations of TC genesis in each phase during the same period are also plotted in Fig. 14. As shown in Fig. 6, the number of TC genesis in IFS is smaller than in NICAM and the observations in spite of the relaxation of the wind speed threshold for the detection of TC in IFS (see Sect. 6). On the other hand, TC genesis in NICAM occurs mainly in a set of phases 3 + 4 where the active convective region associated with MJO resides over the Indian Ocean and the Maritime continent, which is consistent with the observations (Fig. 14a, c). The findings are confirmed more clearly in Fig. 15. The ratio of the number of cyclogenesis in the MJO-active period to that of the whole period indicates that the contribution of MJO to cyclogenesis is prominent in the sets of phases 3 + 4 and 5 + 6 as a whole in Fig. 15c, and this characteristic is well captured in NICAM.

8 Discussion

The phenomena highlighted in this paper include ISO, MJO, and TC, which are the typical rainfall-bearing phenomena in the boreal summer monsoon season. The analysis period for this paper is 3 months for each of 8 years that forms the common target experiment period for both model simulations. The highlights of the discussion are as follows.

8.1 Northward-moving convection associated with ISO in the monsoon season

The ISO-monsoon system is a complex mechanism functioning across the atmosphere, ocean and land over the tropical and sub-tropical regions. The present high-resolution models have limitations in that they are not able to incorporate all the essential physical mechanisms for the ISO in the monsoon season (e.g., air-sea coupling; Oouchi
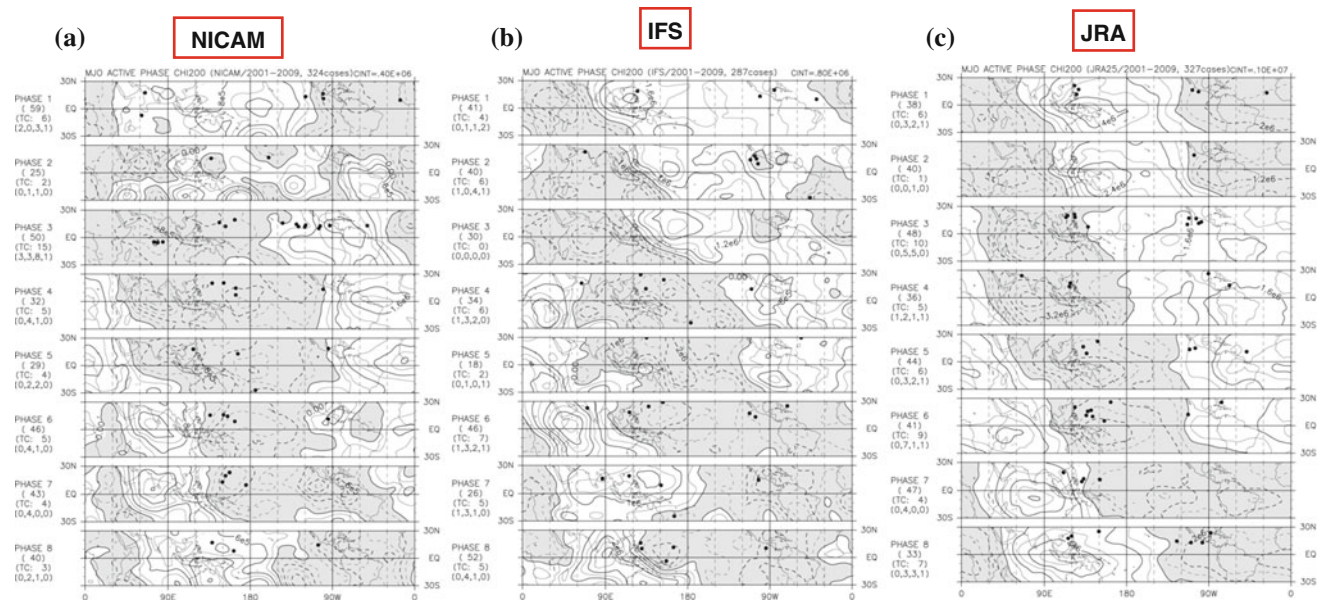
Fig. 14 Composite 200 hPa velocity potential anomalies (*contours*; *shading* for negative values and *solid contours* for positive values) for each phase of the MJO defined in Fig. 8 for the MJO-active period defined in the same method as Taniguchi et al. (2010) for 21 May to 31 July 2001 to 2009 except 2003. *Left* (**a**), *center* (**b**), and *right* (**c**) panels show the results of the NICAM and IFS simulations, and the observations (re-analysis) by JRA/JCDAS analysis, respectively. The total numbers of selected dates for the MJO-active period for figures (**a**), (**b**), and (**c**) are 318, 287, and 336 days, respectively. Contour intervals of (**a**), (**b**), and (**c**) are 0.5×10^6, 0.8×10^6, and 1.0×10^6 (m² s⁻¹), respectively. Also plotted are the locations of TC genesis in each phase (*solid circles*) during the same period. The number of selected days, number of TCs, and number of TCs in each area of ocean (Indian Ocean, West Pacific Ocean, East Pacific Ocean, and Atlantic Ocean) in each phase are listed in parentheses to the left of each phase panel

Fig. 15 The occurrence of TC genesis in each phase of the MJO during the period of 2001–2009 except 2003. *Solid* and *open square bars* indicate the occurrence for the MJO-active period, shown by solid circles in Fig. 14, and the occurrence for the whole period of MJO, respectively. The *left* (**a**), *center* (**b**), and *right* (**c**) columns show the results of the NICAM and IFS simulations, and the observations by IBTrACS, respectively

et al. 2009b), and therefore we do not intend to thoroughly address the issues relating to the monsoon. The aim here is to discuss the present status of the capability of high-resolution models for expressing some atmospheric disturbances in the monsoon region. This is a necessary step towards more comprehensive study in the future.

One of the well-simulated features in NICAM is the northward propagation of cloud clusters (NPCC), which have been demonstrated clearly as a boreal summer intraseasonal disturbance in the season-long simulation (Oouchi et al. 2009b). The importance of NPCC in the weather of the monsoon region is well known (Fu and Wang, 2004).

The propagation of the Indian Ocean NPCC in Project Athena is sometimes obscured by the significant amplitudes of the bias of precipitation and accompanying winds fields. Detailed investigation of NPCC from a meso-scale viewpoint is an appealing research theme.

8.2 MJO

The prior experiments with NICAM have shown that GCRM succeeds in simulating MJO and the associated convections across meso- and synoptic-scales (Miura et al. 2007; Fudeyasu et al. 2008). The Project Athena dataset provides an excellent opportunity to investigate the robustness of the results over multiple boreal summer seasons. To quantify the performance, we conducted an MJO index analysis (Taniguchi et al. 2010) and showed that both IFS and NICAM can simulate some MJO events comparable to observations in terms of its eastward phase propagation, zonal wave number-one feature, and periodicity. It is notable that the peak of the spectrum is detected at about 45 days in NICAM (similar to observation) as most of the existing conventional climate models suffered from a shorter period of MJO compared to observations. Good statistics for the periodicity and strength of MJO were also obtained by a 19-year simulation with the MMF experiment (in which 2-D CRMs at 4-km resolutions are embedded, Khairoutdinov et al. 2008), but the simulation capability was likely to vary among years. The Project Athena model results also have years when the simulated signals of MJO are not consistent with the observations (in terms of phase and amplitude) for a reason we have not yet understood.

8.3 TC: intensity and genesis in association with MJO

TC is such a typical research subject that the high-resolution model can show its benefit. This paper has focused on the comparison of the fundamental characteristics of TC: frequency and intensity, and genesis associated with MJO. We confirm the ability of both models to represent TC intensity by the good relationship between minimum sea-level pressure and maximum surface winds, which is basically consistent with the observations for both IFS and NICAM. Generally, the plot from NICAM is closer to the observations than that for IFS (Fig. 13), which suggests that the size and structure of tropical cyclones in the cloud-resolving model are more comparable to the observations. It is known that even state-of-the-art high-resolution models tend to simulate a lower intensity of low-level wind speeds and a wider radius to maximum winds (Gualdi et al. 2008). This inaccuracy is also reflected in the minimum pressure and maximum wind speed relationship, which is biased toward a lower maximum wind speed for a given

minimum sea level pressure (e.g., Chen and Lin 2011). Therefore, the results from the Athena models that show better relationships are encouraging. Since the intensity forecast is an important research area for future risk assessment that would be inseparable from the projection of TC under a changing climate, the models need to represent the intense classes of TC with sufficient accuracy. The intensity distributions of TCs in IFS are truncated at the higher-end bin compared to observations. This is also true to a lesser degree for NICAM. The 7-km mesh NICAM simulates category 4 TCs and also one case category 5 TC. The result represents an improvement from the prior 14-km mesh NICAM experiment that simulated no category 4 or stronger TCs (Yamada et al. 2010) because of the limited horizontal resolution (Emanuel et al. 2010).

A distinctive key finding is that the high-resolution models used in this study have progressed to represent tropical cyclogenesis that are systematically associated with phases of intra-seasonal signals, in particular of MJO. The result re-confirms the strength of GCRM in capturing this aspect as suggested from the past NICAM simulations based on case studies of particular events (Fudeyasu et al. 2008; Yanase et al. 2010; Oouchi et al. 2009a; Taniguchi et al. 2010). An important finding in these studies is that intra-seasonal control of tropical cyclogenesis by MJO or ISO over the Indian Ocean (Fudeyasu et al. 2008) and the western Pacific (Oouchi et al. 2009a) is more crucial than expected in these regions. The quasi-periodic nature of MJO/ISO will make the forecast of tropical cyclones much more promising, as was previously exemplified by a hydrostatic model (Vitart 2009) and the 25-km mesh non-hydrostatic model (HiRAM) (Chen and Lin 2011). Such intra-seasonal control over tropical cyclogenesis in the Indian Ocean has also been found by an observational study (Kikuchi and Wang 2010), who suggest that monitoring of the evolution of typical ISO during the season may provide a useful medium-range forecast for cyclogenesis there. The results presented in this paper are from the experiment for the boreal summer season when the tropical cyclogenesis over the Indian Ocean is relatively infrequent. We will be able to investigate this aspect in the future by extending the period of simulation over the active tropical cyclone season and increasing the ensemble number.

In summary, the present results point to the importance of the pursuit of tropical cyclogenesis predictability in terms of its systematic link with intra-seasonal phenomena. A plan is underway to develop and apply metrics of ISO and MJO to capture these relationships (Kikuchi and Wang 2010; Taniguchi et al. 2010) and obtain a deeper understanding of the predictability of tropical cyclogenesis. The pursuit of the link between TC genesis and intra-seasonal disturbances has been an elusive area in conventional

climate modeling approaches. GCRM and high-resolution AGCM, as already tried by ECMWF (e.g., Vitart 2009), are expected to promote research and forecast methodology of tropical cyclogenesis.

9 Summary and further implications

High-resolution modeling is generally thought to be a promising way to improve our understanding and prediction of intra-seasonal phenomena. Its effectiveness for the simulation of monsoon-associated atmospheric boreal-summer seasonal features has been reported using the 20-km mesh model (Mizuta et al. 2006; Kusunoki et al. 2006; Kitoh and Kusunoki 2007) within the context of the global hydrostatic model. The pathway taken in Project Athena is distinct and more comprehensive, and provides the first-ever opportunity to make a concerted effort using the 10-km mesh hydrostatic IFS and the 7-km mesh non-hydrostatic NICAM models to examine the capability of high-resolution modeling in the simulation of boreal summer atmospheric disturbances.

The uniqueness of the current project has been the investigation of the performance of high-resolution models for the same target-experiment period in the boreal summer seasons for 8 years (2001–2002, 2004–2009), and exploration of potential issues for model development toward seamless modeling as envisaged by Shukla et al. (2009). The project was realized with the high-end computing resources provided by the National Science Foundation (Kinter et al. 2011). The aim of this paper has been to describe how these models perform in reproducing ISO, MJO and TC, typical phenomena in which convection plays a key role. Discussion of other aspects of the simulation will be found in Kinter et al. (2011). Compared to conventional climate models, an advantage of the high-resolution models used in this study is their capability to explicitly calculate the "multi-scale nature" of phenomena, as their usefulness has been demonstrated by successful sub-seasonal prediction of tropical storms in terms of MJO activity (Vitart 2009) and through a series of NICAM simulations that have benefited from resolving meso-scale convection and their interaction with various tropical disturbances (Satoh et al. 2008). A significant finding of this project is that despite the somewhat persistent bias in the "background" mean field (e.g., precipitation over the Indian Ocean), many characteristics of intra-seasonal disturbances were clearly simulated and to some extentt comparable to observations. These characteristics include ISO over the Indian Ocean, MJO, and its control over tropical cyclogenesis. TCs of high maximum wind intensity and minimum sea level pressure were represented with some fidelity, although the regional distribution was not

replicated well in some basins. It is notable that the averaged periodicity of MJO (about 45 days) in NICAM is close to that of the observations while conventional models tend to have smaller periodicity. The periodicity in IFS is also close to the observations and quite excellent among global hydrostatic models. A main reason for this encouraging result, as demonstrated by prior studies with NICAM, can be related to the capability of the GCRM to resolve an ensemble of deep convective cloud clusters and its interaction with environmental disturbances. IFS benefitted from a dramatic improvement in the representation of MJO recently by changes in convective parameterization (Bechtold et al. 2008), which should account for the good simulation of MJO feature in Project Athena. The ISO is another crucial intra-seasonal mode in the boreal summer season (Kikuchi and Wang 2010). Some models tend to underestimate ISO variances over the Indian monsoon region, and only a few models can realistically capture the evolution and typical horizontal structure of the boreal summer ISO, such as the NW–SE slanted precipitation band (Kim et al. 2007; Sperber and Annamalai 2008). The success of NICAM and IFS in reproducing some ISO features is encouraging.

On the other hand, these intra-seasonal disturbances are influenced by the background climate over the region in question. The climatological mean from both models is poor in the Indian and west Pacific sectors. The precipitation is over-predicted in the tropical region, in particular over the equatorial Indian Ocean and some part of India in NICAM, and especially in the Indo-Pacific sector in IFS. The bias in NICAM is suggested in Oouchi et al. (2009b) and would impede reasonable prediction of tropical cyclogenesis over the Indian Ocean (Yamada et al. 2010) and the monsoon circulation. Efforts are in progress to ameliorate this bias.

Several issues remain in regards to model development in order to make NICAM more accessible for seamless modeling and prediction purposes. An attractive opportunity relevant to Project Athena is to follow through the hypothesis that medium-range prediction of TCs can be significantly improved by the understanding and sophisticated modeling of the disturbances on intra-seasonal time scales (e.g., MJO). Our immediate interest is to pursue the idea of extended prediction of tropical disturbances based on a suitable quantification of their relationship with intra-seasonal disturbances. Toward this goal, an application of metrics analysis such as the MJO index (Wheeler and Hendon 2004; Taniguchi et al. 2010) and BSISO (Kikuchi and Wang 2010) to tropical cyclogenesis is appealing for future work. In Project Athena, we acquired the statistics for a boreal summer dataset of 8 years in length, and by increasing the ensemble number, a more statistically rigorous discussion on the association of the indices with

tropical cyclogenesis can be made, and a basis for future climate projection with a high-resolution model may be obtained. This plan will become viable with the advent of the K-computer, and some plans of a project with NICAM is overviewed at http://www.jamstec.go.jp/hpci-sp/kisyo/kisyo.en.html.

A general issue that Project Athena was unable to investigate with respect to the simulation of MJO and ISO is whether atmosphere–ocean coupling is essential to these disturbances. Vitart et al. (2008) suggested that this coupling may be necessary to improve the score of monthly forecasting of MJO, which is supported by impact of coupling on improving the characteristics of MJO (Rajendran and Kitoh 2006; Vitart et al. 2007), but a strong consensus on this aspect has yet to be reached in the modeling community. This situation is also true for ISO (Fu and Wang 2004) and monsoon simulation (Krishnan et al. 2006). The current status of high-resolution modeling is that model types and the design of experiments are so diverse that a model of a particular design with a different bias in climatology may obtain results somewhat close to observations for the wrong reasons (Sobel et al. 2010), so that the results of these experiments remain inconclusive. The inter-comparison research from a unified framework will be useful to understand the importance of atmosphere–ocean interaction.

Vitart et al. (2007) argued that the success of MJO simulation depends on the initial condition, and, specifically, the location of convection that drives MJO is suggested to be important (Vitart et al. 2007). This is reasonable as convection is closely associated with the behavior of MJO (Madden and Julian 1972). We cannot discriminate the skill of MJO prediction inherent to the model from the associated favorable components that can be included in the given initial condition of each Athena model. As opposed to the differences in model types and physics involved, those in the initial conditions can have a different response of each model atmosphere in the realization of the propagation of MJO. This issue will become more important if the model is used in forecast mode in the future. A more systematic understanding of this problem requires further ensemble simulations and computational resources, which will be available in the near future. It remains controversial whether the 7-km grid spacing is acceptable for simulations without cumulus parameterization. It would be desirable to use a finer grid spacing, such as 1 km or less, if sufficient computational resources are available. Through the series of past research with NICAM, we have demonstrated that the use of the 7-km grid spacing does not degrade the focus of the discussion with respect to synoptic control over cloud clusters or cloud ensembles that are pertinent to tropical cyclogenesis, the behavior of MJO, and monsoon-associated disturbances (Miura et al.

2007; Oouchi et al. 2009b; Taniguchi et al. 2010). The 25-km mesh non-hydrostatic model also demonstrated a skillful seasonal prediction of tropical cyclones over the Atlantic for a 10-year period, although it seemed to underpredict the intense TCs (Chen and Lin 2011). The use of the 7-km mesh NICAM and 10-km mesh IFS in this project would therefore be acceptable for the current purpose of the research that has focused mainly on intra-seasonal synoptic-scale events and their interaction with sub-synoptic-scale convection systems. The issue on model resolution from around 1–10 km is recently noted as the so-called 'grey zone' (Gerard et al. 2009), and the coordination of the Grey Zone Project was discussed at the 26th Session of the CAS/JSC Working Group on Numerical Experimentation (WGNE-26, 18–22 October 2010, Tokyo, Japan; http://www.wmo.int/pages/about/sec/rescrosscut/resdept_wgne.html).

A possible future pathway from Project Athena is to narrow the uncertainties of future climate projection with high-resolution AGCMs. Experiments with IFS with two different resolutions (16 and 125-km) showed that the regional precipitation change over Europe is projected to vary between the resolutions, and hence that higher resolution simulations are required given their increased fidelity to the observations (Kinter et al. 2011). The study here has taken an initial step by assessing simulations of key phenomena of intra-seasonal time scales. The first challenge of the GCRM to give an insight into the future change of tropical cyclones was reported by Yamada et al. (2010) from a suite of 14-km mesh time-slice experiments with NICAM. They discussed possible change in the cloud height of TCs as well as the general statistics of frequency, intensity, and environmental factors for TCs. The discussion of the change in the cloud height was unable to be developed using traditional hydrostatic models, and therefore it is appealing to make use of the strengths of the GCRM dataset. An extension of this type of future projection research with the GCRM will be important in mitigating the uncertainties in traditional GCMs for projecting future change of intra-seasonal disturbances: TC, MJO, and ISO, that may cause a change in hazardous risk given a secular change of the background climate. Project Athena serves as a good incentive to shape the direction of such research.

References

Annamalai H, Slingo JM (2001) Active/break cycles: diagnosis of the intraseasonal variability of the Asian summer monsoon. Clim Dyn 18:85–102

Atkinson GD, Holliday CR (1977) Tropical cyclone minimum sea level pressure/maximum sustained wind relationship for the western north Pacific. Mon Weather Rev 105:421–427

Bechtold P, Koehler M, Jung T, Doblas-Reyes P, Leutbecher M, Rodwell M, Vitart F (2008) Advances in simulating atmospheric variability with the ECMWF model: from synoptic to decadal time-scales. QJR Meteorol Soc 134:1337–1351. doi:10.1002/qj.289

Benedict JJ, Randall DA (2009) Structure of the Madden–Julian oscillation in the superparameterized CAM. J Atmos Sci 66:3277–3296

Camargo SJ, Wheeler MC, Sobel AH (2009) Diagnosis of the MJO modulation of tropical cyclogenesis using an empirical index. J Atmos Sci 66:3061–3074. doi:10.1175/2009JAS3101.1

Chen JH, Lin SJ (2011) The remarkable predictability of inter-annual variability of Atlantic hurricanes during the past decade Geophys Res Lett (in press). doi:10.1029/2011GL047629

Chikira M, Sugiyama M (2010) A cumulus parameterization with state-dependent entrainment rate. Part I: description and sensitivity to temperature and humidity profiles. J Atmos Sci 67:2171–2193

Dirmeyer PA, Cash B, Kinter III A, Jung JL, Marx TL, Satoh M, Stan C, Tomita H, Towers P, Wedi N, Achuthavarier D, Adams JM, Altshule EL, Huang B, Jin EK, Manganello J (2011) Simulating the hydrologic diurnal cycle in global climate models: resolution versus parameterization. Clim Dyn (accepted). doi:10.1007/s00382-011-1127-9

Emanuel K, Oouchi K, Satoh M, Tomita H, Yamada Y (2010) Comparison of explicitly simulated and downscaled tropical cyclone activity in a high-resolution global climate model. J Adv Model Earth Syst 2, Art. #9, 9 pp. doi:10.3894/JAMES.2010.2.9

Flatau MK, Flatau PJ, Rudnick D (2001) The dynamics of double monsoon onsets. J Clim 14:4130–4146

Fu X, Wang B (2004) Differences of boreal-summer intraseasonal oscillations simulated in an atmosphere-ocean coupled model and an atmosphere-only model. J Clim 17:1263–1271

Fudeyasu H, Wang Y, Satoh M, Nasuno T, Miura H, Yanase W (2008) The global cloud-system-resolving model NICAM successfully simulated the lifecycles of two real tropical cyclones. Geophys Res Lett 35:L22808. doi:10.1029/2008GL0360033

Gerard L, Piriou JM, Brozkova R, Geleyn JF, Banciu D (2009) Cloud and precipitation parameterization in a Meso-Gamma-Scale operational weather prediction model. Mon Weather Rev 137:3960–3977

Goswami BN, Krishnamurthy V, Annamalai H (1999) A broad scale circulation index for the interannual variability of the Indian summer monsoon. Q J R Meteorol Soc 125:611–633

Gottschalck J, Wheeler M, Weickmann K, Vitart F, Savage N, Lin H, Hendon H, Waliser D, Sperber K, Nakagawa M, Prestrelo C, Flatau M, Higgins W (2010) A framework for assessing operational Madden–Julian oscillation forecasts, a CLIVAR MJO Working Group Project. Bull Am Meteorol Soc 81:1247–1258

Gualdi S, Scoccimarro E, Navarra A (2008) Changes in tropical cyclone activity due to global warming: results from a high-resolution coupled general circulation model. J Clim 21:5204–5228

Iga S, Tomita H, Satoh M, Goto K (2007) Mountain-wave-like spurious waves associated with simulated cold fronts due to inconsistencies between horizontal and vertical resolutions. Mon Weather Rev 135:2629–2641

Inoue T, Satoh M, Hagihara Y, Miura H, Schmetz J (2010) Comparison of high-level clouds represented in a global cloud-system resolving model with CALIPSO/CloudSat and geostationary satellite observations. J Geophys Res 115:D00H22

IPCC 2007: Climate change (2007) The physical science basis. In: Contribution of Working Group I to the 4th Assessment Report of the Intergovernmental Panel on Climate Change. Cambridge University Press, Cambridge, 996 pp

Jung T, Balsamo G, Bechtold P, Beljaars ACM, Kohler M, Miller MJ, Morcrette JJ, Orr A, Rodwell MJ, Tompkins AM (2010) The ECMWF model climate: recent progress through improved physical parametrizations. Q J R Meteorol Soc 136:1145–1160

Kawamura R (1998) A possible mechanism of the Asian summer monsoon-ENSO coupling. J Meteorol Soc Jpn 76:1009–1027

Kemball-Cook S, Wang B (2001) Equatorial waves and air–sea interaction in the Boreal summer intraseasonal oscillation. J Clim 14:2923–2942

Khairoutdinov MF, DeMotte C, Randall DA (2008) Evaluation of the simulated interannual and subseasonal variability in an AMIP-Style simulation using the CSU multiscale modeling framework. J Clim 21:413–431

Kikuchi K, Wang B (2010) Formation of tropical cyclones in the Northern Indian Ocean associated with two types of tropical intraseasonal oscillation modes. J Meteorol Soc Jpn 88:475–496

Kim HM, Kang IS, Wang B, Lee JY (2007) Interannual variations of the Boreal summer intraseasonal variability predicted by ten atmosphere-ocean coupled models. Clim Dyn 23:5–7. doi:10.1007/s00382-007-0292-3

Kim D, Sperber K, Stern W, Waliser D, Kang IS, Maloney E, Wang W, Weickmann K, Benedict J, Khairoutdinov M, Lee MI, Neale R, Suarez M, Thayer-Calder K, Zhang G (2009) Application of MJO simulation diagnostics to climate models. J Clim 22:6413–6436

Kinter JL III, Cash B, Achuthavarier D, Adams J, Altshuler E, Dirmeyer P, Doty B, Huang B, Marx L, Manganello J, Stan C, Wakefield T, Jin E, Palmer T, Hamrud M, Jung T, Miller M, Towers P, Wedi N, Satoh M, Tomita H, Kodama C, Nasuno T, Oouchi K, Taniguchi H, Andrews P, Baer T, Ezell M, Halloy C,

John D, Loftis B, Mohr R, Wong K (2011) Revolutionizing climate modeling—Project Athena: a multi-institutional international collaboration (submitted)

Kitoh A, Kusunoki S (2007) East Asian summer monsoon simulation by a 20-km mesh AGCM. Clim Dyn 31:389–401

Knaff KR, Kruk MC, Levinson DH, Diamond HJ, Neumann CJ (2010) The international best track archive for climate stewardship (IBTrACS) unifying tropical cyclone data. Bull Am Meteorol Soc 91:363–376

Krishnan R, Ramesh KV, Samala BK, Meyers G, Slingo JM, Fennessy MJ (2006) Indian Ocean-monsoon coupled interactions and impending monsoon droughts. Geophys Res Lett 33:L08711. doi:10.1029/2006GL025811

Kusunoki S, Yoshimura J, Yoshimura H, Noda A, Oouchi K, Mizuta R (2006) Change of Baiu rain band in global warming projection by an atmospheric general circulation model with a 20-km grid size. J Meteorol Soc Jpn 84:581–611

Lau KM, Chan PH (1986) Aspects of the 40–50 day oscillation during the northern summer as inferred from outgoing longwave radiation. Mon Weather Rev 114:1354–1367

Liebmann B, Hendon HH, Glick JD (1994) The relationship between tropical cyclones of the western Pacific and Indian Oceans and the Madden–Julian oscillation. J Meteorol Soc Jpn 72:401–412

Lin JL, Kiladis GN, Mapes BE, Weickmann KM, Sperber KR, Lin W, Wheeler MC, Schubert SD, Del Genio A, Donner LJ, Emori S, Gueremy JF, Hourdin F, Rasch PJ, Roeckner E, Scinocca JF (2006) Tropical intraseasonal variability in 14 IPCC AR4 climate models. Part I: Convective signals. J Clim 19:2665–2690. doi:10.1175/JCLI3735.1

Liu P, Satoh M, Wang B, Fudeyasu H, Nasuno T, Li T, Miura H, Taniguchi H, Masunaga H, Fu X, Annamalai H (2009) An MJO simulated by the NICAM at 14-km and 7-km resolutions. Mon Weather Rev 137:3254–3268

Louis JF (1979) A parametric model of vertical eddy fluxes in the atmosphere. Bound Layer Meteorol 17:187–202

Madden RA, Julian PR (1972) Description of global-scale circulation cells in the tropics with a 40–50 day period. J Atmos Sci 29:1109–1123

Manganello JV, Hodges KI, Kinter III JL, Cash BA, Marx L, Jung T, Achuthavarier D, Adams JM, Altshuler EL, Huang B, Jin EK, Stan C, Towers P, Wedi P (2011) Tropical cyclone climatology in a 10-km global atmospheric GCM: Toward weather-resolving climate modeling (in preparation)

Masunaga H, Satoh M, Miura H (2008) A joint satellite and global CRM analysis of an MJO event: model diagnosis. J Geophys Res Atmos 113:D17210

Miura H, Satoh M, Nasuno T, Noda AT, Oouchi K (2007) An Madden–Julian Oscillation event simulated using a global cloud-resolving model. Science 318:1763–1765

Mizuta R, Oouchi K, Yoshimura H, Noda A, Katayama K, Yukimoto S, Hosaka M, Kusunoki S, Kawai H, Nakagawa M (2006) 20 km-mesh global climate simulations using JMA-GSM model—mean climate states. J Meteorol Soc Jpn 84:165–185

Nakanishi M, Niino H (2006) An improved mellor-yamada level-3 model: its numerical stability and application to a regional prediction of advection fog. Bound Layer Meteorol 119:397–407

Nakazawa T (1988) Tropical super clusters within intraseasonal variations over the western Pacific. J Meteorol Soc Jpn 66:823–839

Nasuno T, Tomita H, Iga S, Miura H, Satoh M (2007) Multi-scale organization of convection simulated with explicit cloud processes on an aquaplanet. J Atmos Sci 64:1902–1921

Nasuno T, Miura H, Satoh M, Noda AT, Oouchi K (2009) Multi-scale organization of convection in a global numerical simulation of the December 2006 MJO event using explicit moist processes. J Meteorol Soc Jpn 87:335–345

Noda AT, Oouchi K, Satoh M, Tomita H, Iga S, Tsushima Y (2010) Importance of the subgrid-scale turbulent moist process: cloud distribution in global cloud-resolving simulations. Atmos Res 96:208–217

Onogi K, Tsutsui J, Koide H, Sakamoto M, Kobayashi S, Hatsushika H, Matsumoto T, Yamazaki N, Kamahori H, Takahashi K, Kadokura S, Wada K, Kato K, Oyama R, Ose T, Mannoji N, Taira R (2007) The JRA-25 reanalysis. J Meteorol Soc Jpn 85:369–432

Oouchi K, Yoshimura J, Yoshimura H, Mizuta R, Kusunoki S, Noda A (2006) Tropical cyclone climatology in a global-warming climate as simulated in a 20-km-mesh global atmospheric model: frequency and intensity analysis. J Meteorol Soc Jpn 84:259–276

Oouchi K, Noda AT, Satoh M, Miura H, Tomita H, Nasuno T, Iga SI (2009a) A simulated preconditioning of typhoon genesis controlled by a boreal summer Madden–Julian Oscillation event in a global cloud-resolving mode. SOLA 5:65–68. doi:10.2151/sola.2009.017

Oouchi K, Noda AT, Satoh M, Wang B, Xie SP, Takahashi H, Yasunari T (2009b) Asian summer monsoon simulated by a global cloud-system resolving model: diurnal to intra-seasonal variability. Geophys Res Lett 36:L11815. doi:10.1029/2009GL038271

Parthasarathy B, Munot AA, Kothawale DR (1994) All India monthly and seasonal rainfall series: 1871–1993. Theor Appl Climatol 49:217–224

Rajendran K, Kitoh A (2006) Modulation of tropical intraseasonal oscillations by ocean–atmosphere coupling. J Clim 19:366–391

Rashid HA, Hendon HH, Wheeler MC, Alves O (2011) Prediction of the Madden–Julian oscillation with the POAMA dynamical prediction system. Clim Dyn 36:649–661. doi:10.1007/s00382-010-0754-x

Reynolds RW, Rayner NA, Smith TM, Stokes TC, Wang WQ (2002) An improved in situ and satellite SST analysis for climate. J Clim 15:1609–1625

Reynolds RW, Smith TM, Liu C, Chelton DB, Casey KS, Schlax MG (2007) Daily high-resolution-blended analyses for sea surface temperature. J Clim 20:5473–5496

Sato T, Miura H, Satoh M, Takayabu YN, Wang Y (2009) Diurnal cycle of precipitation in the tropics simulated in a global cloud-resolving model. J Clim 22:4809–4826. doi:10.1175/2009JCLI2890.1

Satoh M, Matsuno T, Tomita H, Miura H, Nasuno T, Iga S (2008) Nonhydrostatic Icosahedral Atmospheric Model (NICAM) for global cloud resolving simulations. J Comput Phys 227:3486–3514. doi:10.1016/j.jcp.2007.02.006

Sekiguchi M, Nakajima T (2008) A k-distribution-based radiation code and its computational optimization for an atmospheric general circulation model J. Quant Spectrosc Radiat Transf 109:2779–2793

Shukla J, Hagedorn R, Hoskins B, Kinter J, Marotzke J, Miller M, Palmer TN, Slingo J (2009) Strategies: revolution in climate prediction is both necessary and possible: a declaration at the world modeling summit for climate prediction. Bull Am Meteorol Soc 90:16–19

Sikka DR, Gadgil S (1980) On the maximum cloud zone and the ITCZ over Indian longitudes during the southwest monsoon. Mon Weather Rev 108:1840–1853

Skamarock WC (2004) Evaluating mesoscale NWP models using kinetic energy spectra. Mon Weather Rev 132:3019–3032

Slingo JM et al (1996) Intraseasonal oscillation in 15 atmospheric general circulation models: results from an AMIP diagnostic subproject. Clim Dyn 12:325–357. doi:10.1007/BF00231106

Sobel AH, Maloney ED, Bellon G, Frierson DM (2010) Surface fluxes and tropical intraseasonal variability: a reassessment. J Adv Model Earth Syst 2, Art 2, 27 pp. doi:10.3894/JAMES.2010.2.2

Sperber KR, Annamalai H (2008) Coupled model simulations of boreal-summer intraseasonal (30–50-day) variability, part II: systematic errors and caution on use of metrics. Clim Dyn 31:345–372

Stan S, Khairoutdinov M, DeMott CA, Krishnamurthy V, Straus DM, Randall DA, Kinter JL III, Shukla J (2009) An ocean-atmosphere climate simulation with an embedded cloud-resolving model. Geophys Res Lett 37:L01702. doi:10.1029/2009GL040822

Takata K, Emori S, Watanabe S (2003) Development of the minimal advanced treatments of surface interaction and runoff. Glob Planet Change 38:209–222

Taniguchi H, Yanase W, Satoh M (2010) Ensemble simulation of cyclone Nargis by a global cloud-system-resolving model - modulation of cyclogenesis by the Madden–Julian Oscillation. J Meteorol Soc Jpn 88:571–591

Tiedtke M (1989) A comprehensive mass flux scheme for cumulus parameterization in large-scale models. Mon Weather Rev 117:1779–1800

Tomita H (2008) New microphysics with five and six categories with diagnostic generation of cloud ice. J Meteorol Soc Jpn 86A:121–142

Tomita H, Satoh M (2004) A new dynamical framework of nonhydrostatic global model using the icosahedral grid. Fluid Dyn Res 34:357–400

Tomita H, Miura H, Iga S, Nasuno T, Satoh M (2005) A global cloud-resolving simulation: preliminary results from an aqua planet experiment. Geophys Res Lett 32:L08805. doi:10.1029/2005GL022459

Vitart F (2009) Impact of the Madden Julian Oscillation on tropical storms and risk of landfall in the ECMWF forecast system. Geophys Res Lett 36:L15802. doi:10.1029/2009GL039089

Vitart F, Woolnough S, Balmaseda MA, Tompkins A (2007) Monthly forecast of the Madden–Julian Oscillation using a coupled GCM. Mon Weather Rev 135:2700–2715. doi:10.1175/MWR3415.1

Vitart F, Buizza R, Alonso Balmaseda M, Balsamo G, Bidlot JR, Bonet A, Fuentes M, Hofstadler A, Moleni F, Palmer T (2008) The new VAREPS-monthly forecasting system: a first step towards seamless prediction. Q J R Meteorol Soc 134:1789–1799. doi:10.1002/qj.322

Waliser DE, Jin K, Kang IS, Stern WF, Schubert SD, Wu MLC, Lau KM, Lee MI, Krishnamurthy V, Kitoh A, Meehl GA, Galin VY, Satyan V, Mandke SK, Wu G, Liu Y, Park CK (2003) AGCM simulations of intraseasonal variability associated with the Asian summer monsoon. Clim Dyn 21:423–446. doi:10.1007/s00382-003-0337-1

Walsh KJE, Fiorino M, Landsea CW, McInnes KL (2007) Objectively determined resolution-dependent threshold criteria for the detection of tropical cyclones in climate models and reanalyses. J Clim 20:2307–2314

Wang B, Fan Z (1999) Choice of South Asian summer monsoon indices. Bull Am Meteorol Soc 80:629–638

Wang B, Rui H (1990) Synoptic climatology of transient tropical intraseasonal convection anomalies: 1975–1985. Meteorol Atmos Phys 44:43–61

Wang B, Wu R, Lau KM (2001) Interannual variability of Asian summer monsoon: contrast between the Indian and western North Pacific-East Asian monsoons. J Clim 14:4073–4090

Webster PJ, Yang S (1992) Monsoon and ENSO: selectively interactive systems. Q J R Meteorol Soc 118:877–926

Wheeler MC, Hendon HH (2004) An all-season real-time multivariate MJO index: development of an index for monitoring and prediction. Mon Weather Rev 132:1917–1932

Wheeler MC, Kiladis GN (1999) Convectively coupled equatorial waves: analysis of clouds and temperature in the wavenumber–frequency domain. J Atmos Sci 56:374–399

Yamada Y, Oouchi K, Satoh M, Tomita H, Yanase W (2010) Projection of changes in tropical cyclone activity and cloud height due to greenhouse warming: global cloud-system-resolving approach. Geophys Res Lett 37:L07709. doi:10.1029/2010GL042518

Yanase W, Taniguchi H, Satoh M (2010) Environmental modulation and numerical predictability associated with the genesis of tropical cyclone Nargis (2008). J Meteorol Soc Jpn 88:497–519

Yasunari T (1979) Cloudiness fluctuations associated with the northern hemisphere summer monsoon. J Meteorol Soc Jpn 57:227–242

Yasunari T (1980) A quasi-stationary appearance of 30–40 day period in the cloudiness fluctuations during the summer monsoon over India. J Meteorol Soc Jpn 58:225–229

Yokoi S, Takayabu YN, Chan JCL (2009) Tropical cyclone genesis frequency over the western North Pacific simulated in medium-resolution coupled general circulation models. Clim Dyn 33:665–683. doi:10.1007/s00382-009-0593-9